LA-12870-MS

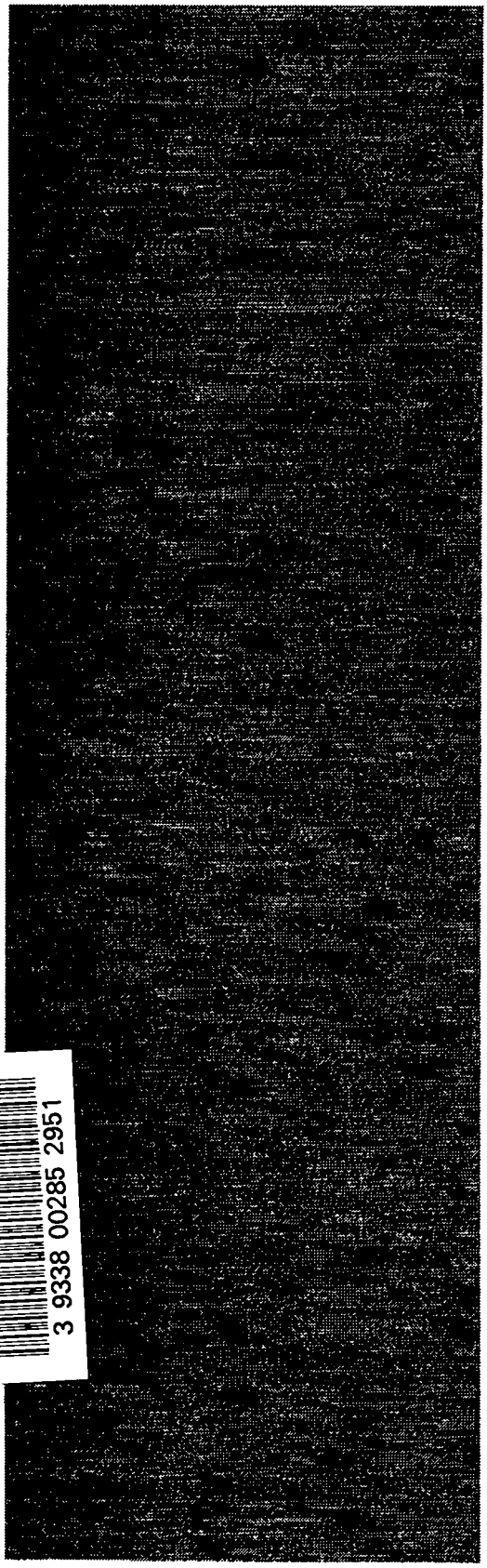

Far-Field Fast-Neutron Energy Spectra from an Unshielded Fission Reactor

Los Alamos
NATIONAL LABORATORY

Los Alamos National Laboratory is operated by the University of California for the United States Department of Energy under contract W-7405-ENG-36.

Edited by Martha Lee DeLanoy, Group CIC-1
Photocomposition by Wendy Burditt, Group CIC-1

This work was supported by the U.S. Department of Energy, Research and Technology Division, Office of Nonproliferation and National Security.

An Affirmative Action/Equal Opportunity Employer

LA-12870-MS

UC-700
Issued: March 1995

Far-Field Fast-Neutron Energy Spectra from an Unshielded Fission Reactor

R. C. Byrd
G. P. Estes
C. R. Mannon*

*Teacher Research Associate at Los Alamos

Los Alamos
NATIONAL LABORATORY
Los Alamos, New Mexico 87545

FAR-FIELD FAST-NEUTRON ENERGY SPECTRA FROM AN UNSHIELDED FISSION REACTOR

by

R. C. Byrd, G. P. Estes, and C. R. Mannon

ABSTRACT

To a large extent, radiation exposure, radiation measurements, and radiation protection factors depend upon the assignment of doses to the survivors of the nuclear bombings of Hiroshima and Nagasaki. For neutrons, the problem of correlating dose with fluence inevitably leads to questions about air-over-ground transport calculations, which have been tested primarily against benchmark measurements using the reactor at the Army Pulse Radiation Facility at Aberdeen Proving Ground, Maryland. At the ranges of 1000–2000 m that are most relevant for the Hiroshima survivors, the agreement between the calculated and measured integral dose values is generally within 10%, but comparisons of the differential values differ by as much as 40%. Using a new type of neutron spectrometer, we report measured neutron energy spectra from 0.5 to 10 MeV at distances of 1080 m and 1620 m, with results that generally confirm those of other experiments. Based on studies of transmission "windows" through nitrogen/oxygen mixtures and the effect of scattering from the ground near the detector, calculations that take into account the detector surroundings and use ENDF/B-VI cross sections are able to obtain agreement within 20% at almost all energies.

---

1. INTRODUCTION: NEUTRON DOSIMETRY

Hiroshima Studies. The basis for much of radiation dosimetry is the epidemiological studies of the survivors of the nuclear detonations at Hiroshima and Nagasaki. These studies provide the necessary empirical correlations between range, shielding factors, and biological effects.[1] For estimating exposure in other situations, these correlations must be expressed as the dose at each location in terms of radiation types, intensities, and energies—that is, the spectra of penetrating gamma rays and neutrons. For neutrons, the on-site data consist of two types of activation measurements obtained after the fact. Although most of the neutron dose is produced at high energies, activation products from fast neutrons are short-lived; accordingly, fast-neutron measurements exist only at short ranges, where there are few survivors.[2] On the other hand, the activation products at larger ranges have longer half-lives, but they are generally the result of neutron capture at thermal energies, where there is little biological effect.[2,3] Thus, deriving useful estimates of the neutron dose received by the survivors requires the use of radiation-transport calculations that connect the fast-neutron data at short range with the thermal-neutron data at long range, in the process providing neutron spectra and hence estimated doses at all ranges. In practice, such calculations originate from source spectra provided by weapons-design

codes and tested against subsequent measurements on realistic mockups.[4] Unfortunately, however, this approach has been unable to provide a consistent reproduction of the various activation measurements.[5]

Benchmark Studies. Because air-over-ground radiation transport is a critical link in all the studies, several attempts have been made to provide independent benchmarks of the calculations under conditions similar to those at Hiroshima and Nagasaki.[1] In particular, measurements and calculations have been made of the neutron fluence observed at ranges of 100–2000 m from the unshielded reactor at the Army Pulse Radiation Facility (APRF) at Aberdeen Proving Ground in Aberdeen, Maryland,[6] which should provide an environment similar to that at Hiroshima. As part of this program, this report presents high-resolution measurements of neutron spectra from 0.5 to 10 MeV for two of the longest distances available, 1080 m and 1620 m. Spectral data at these ranges provide a valuable benchmark for the transport codes that are used for determining the radiation dose directly or for calculating the scattering of neutrons to lower energies, as required for interpreting the activation data at Hiroshima and Nagasaki. We therefore include in our analyses representative comparisons with other measurements and calculations.

Neutron Spectroscopy. The key to our measurements is an instrument originally developed at Los Alamos National Laboratory (LANL) to provide fast-neutron spectra in the energy range from 1 to 20 MeV.[7–9] The technology is based on a special type of boron-loaded plastic scintillator that provides a unique signature for fast neutrons that have deposited all their energy in the detector. This approach has several potential advantages over the techniques previously used for spectral measurements. (1) Neutron events are identified unambiguously, with all nonneutron backgrounds completely eliminated; (2) a built-in calibration function helps to ensure the reliability of the measurements; and (3) the energies of the incident neutrons can be determined with good resolution (20–40%) and a minimum of processing. In addition, (4) the multielement segmentation of the detector provides some information about the direction of the incident flux. The prototype detector used for the present measurements is currently being reengineered into a portable version (the Field Neutron Spectrometer, or FNS) to allow such spectral data to be obtained routinely.

Contents. Section 2 uses examples from laboratory calibrations to explain the neutron detector's operation; readers already familiar with the instrument from earlier studies[7,8] may choose to skim over this explanation. Section 3 describes the data obtained specifically for the APRF dosimetry study and compares the results with other measurements, including integral doses. Section 4 uses calculations to establish the systematic behavior of the long-range transport problem, and Sec. 5 presents a summary and conclusions.

2. DETECTOR PRINCIPLES

Borated-Plastic Neutron Spectrometers. The traditional methods for making spectral measurements of neutron fluxes in the 1- to 10-MeV range use either neutron scattering in an organic scintillator[10,11] or neutron capture in moderated detectors of different sizes.[12] In either case the measurements must be unfolded to recover the energy distribution of the incident neutrons. To provide an alternative, LANL developed a new type of fast-neutron spectrometer[13] based on the boron-loaded plastic scintillator BC454 made by Bicron Corporation of Newbury, Ohio. Because the active element is a solid plastic, such a detector is inherently rugged and can be readily operated over the wide temperature ranges typical of field operations. Its capabilities have previously been exploited in several applications,[8,14,15] and a suitable instrument, the backup unit for the Army Background Experiment[7] (ABE), was available for this project. This detector is large enough to provide

a reasonable counting rate, and much of its hardware and software was readily adaptable for field use. As shown in **Fig. 2.1**, the instrument head consists of four BC454 scintillator rods with photomultiplier tubes at each end, as well as the electronics needed for high-voltage (HV) power supplies and preamplifiers. The four side-by-side scintillator elements are also able to provide some indication of the direction of the incident neutron flux.[16,17] Thus, the detector actually provides two types of neutron information, spectroscopy and directionality. (Readers already familiar with the operation of the instrument may choose to skip to Sec. 3.)

Time-Difference Spectrum. The detector's first important feature, the selection of fast neutrons, relies on an identifying sequence of two scintillator pulses, usually labelled as the *S1* and *S2* pulses.[13] The first pulse is produced by elastic scattering of the incident neutron from the protons in the $(CH)_n$ plastic material; the second comes from the subsequent capture of the moderated neutron by the boron added to the scintillator. Specific criteria are used to isolate these neutron scatter-and-capture events from other backgrounds. One feature is derived from the characteristic time interval between the two pulses. A clock in the electronics measures this time difference; for neutron-capture events, the distribution of these differences T should have an approximately exponential shape $N(T) \propto \exp(-T/\tau)$.[9] Given the amount of boron in our scintillator, the time constant τ should be about 2 μs.[7,9] **Figure 2.2** shows a logarithmic time spectrum measured with a laboratory ^{252}Cf source located 2 m to the side of the detector and facing one pair of rods. The solid histogram ("Raw Data") shows the accumulated counts at each time difference T. The dashed and dotted lines identify the two major components of the spectrum, labelled "Random Bkgnd"

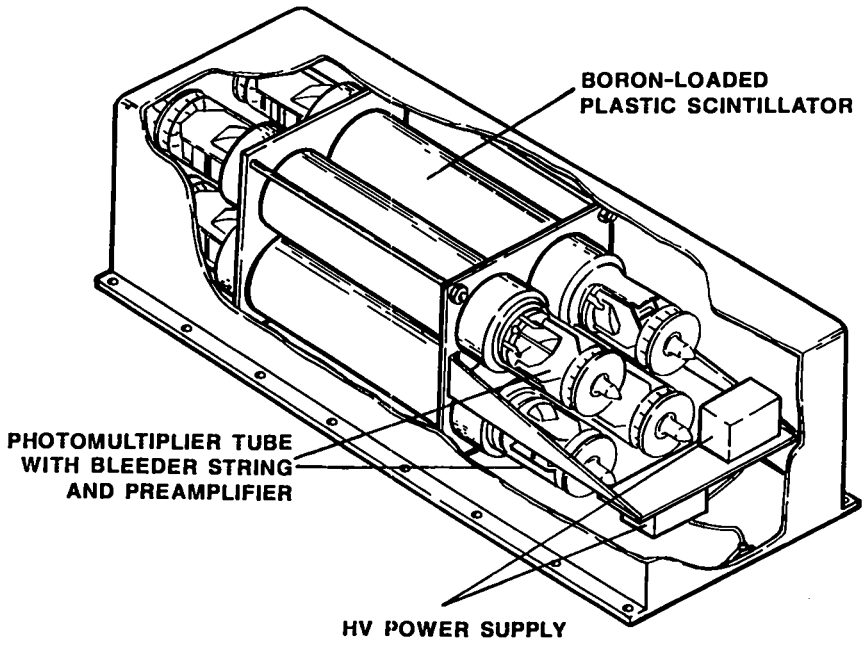

Fig. 2.1. Cutaway view of the neutron spectrometer. Four scintillator rods, each with two photomultiplier tubes, provide energy spectra and an indication of the direction of the incident neutrons. Most of the electronics is contained in a separate package (not shown).

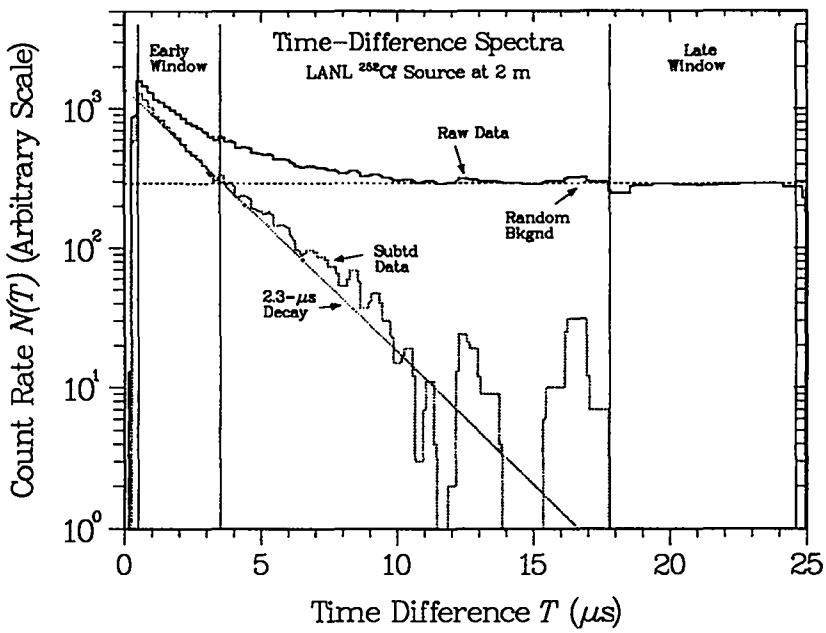

Fig. 2.2. Analysis of a time-difference spectrum measured with a laboratory ^{252}Cf source placed 2 m from the detector. Most of the counts in the raw data are caused either by neutron recoil-and-capture events (the 2.3-μs line) or by random coincidences (the constant level). The time windows are used to select two specific sets of events for further processing.

and "2.3-μs Decay." At the longest times, about five or so time constants, further neutron capture is very unlikely, and the count rate is dominated by an almost constant background of random coincidences, that is, first and second pulses that are produced by uncorrelated neutrons or gamma rays. Subtracting this constant rate from the raw data gives a corrected result ("Subtd Data") that agrees well with the expected 2.3-μs capture rate, especially for the first few time constants. The additional events in the subtracted data at intermediate times are possibly caused by scattering between the different scintillator rods. This subtraction demonstrates a major signature of fast-neutron capture in the detector, the exponential time dependence of the corrected count rate.

Light-Output Distributions. Further analysis of the data focuses on events with second (*S2*) pulses that fall in two particular regions of the time-difference spectrum in Fig. 2.2. In the "late" window, the observed coincidences are almost entirely from random background; in the "early" window, the added coincidences closely follow the expected time signature for neutron-capture events. The light-output spectra for events in these two windows are shown in **Fig. 2.3a**; each has been averaged over all four rods and plotted on a scale calibrated in keV_{ee}, meaning "keV electron equivalent." This light-output scale is needed because scintillators saturate and become nonlinear at the large energy densities of slower or heavier particles, including recoil protons at low energies. Because energetic electrons are the least-ionizing particles—and their response is therefore the most linear—the light output for other particles is conventionally expressed in units of electron energy, hence keV_{ee}. This scale is usually established by measuring Compton electron spectra for gamma rays at different energies. In our case, the reaction products from the boron-capture reaction provide an internal calibration for the instrument, as discussed next.

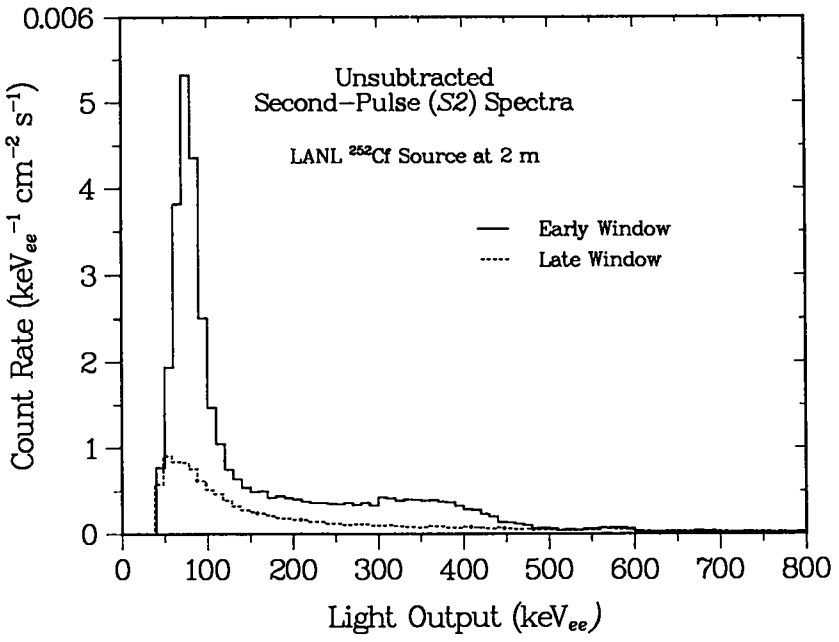

Fig. 2.3a. Unsubtracted light-output spectra for events with second (*S2*) pulses in the early and late time windows indicated in Fig. 2.2.

Second-Pulse Capture Spectra. The *S2* spectra in Fig. 2.3a provide another criterion for neutron detection. The nearly featureless spectrum for the late window (dashed line) is composed of a variety of backgrounds (gamma rays, low-energy neutrons, and escaping fast neutrons); usually, no single type of radiation is identifiable. Subtracting this background from the spectrum for the early window gives the result shown in **Fig. 2.3b**, which has a very specific form. The $^{10}B(n,\alpha)^{7}Li$ capture reaction usually produces a 1.5-MeV alpha particle, a 0.8-MeV ^{7}Li ion, and a 478-keV gamma ray from the decay of the first excited state of ^{7}Li to its ground state. The energies of the recoiling alpha and ^{7}Li particles are always absorbed, but the resulting light output is only 93 keV$_{ee}$ because of the saturation in the energy-to-light conversion. If the 478-keV gamma ray undergoes Compton scattering before escaping, it can deposit as much as 311 keV of additional energy. Counts in the peak correspond to detection of only the recoil alpha and ^{7}Li ions with complete escape of the gamma ray, and the long shoulder results from adding as much as 311 keV from the Compton electron. Thus, the Compton edge should be shifted to appear at (311 + 93 = 404) keV$_{ee}$. This definite spectral shape not only gives another key criterion for neutron selection, it also provides a two-point internal calibration for the detector's light-output scale, the second important feature of boron-loaded scintillators.

Background Response. A different laboratory experiment demonstrates the detector's rejection of events not caused by incident fast neutrons. **Figure 2.4a** shows the time-difference spectrum measured at LANL with the calibration sources removed. In this case the random background is almost identical with the raw data; any curve assigned to the 2.3-μs capture rate is lower by about an order of magnitude. **Figure 2.4b** shows the resulting *S2* distributions for the early and late windows; as expected from the time spectrum, they are almost identical. Their subtraction (not shown) leaves a small but clear capture peak with a hint of a Compton edge. Our conclusion is that the room background is mostly gamma rays, but there is a small component of fast neutrons produced by cosmic-ray interactions. All backgrounds not from fast neutrons—that is, gamma rays, low-energy

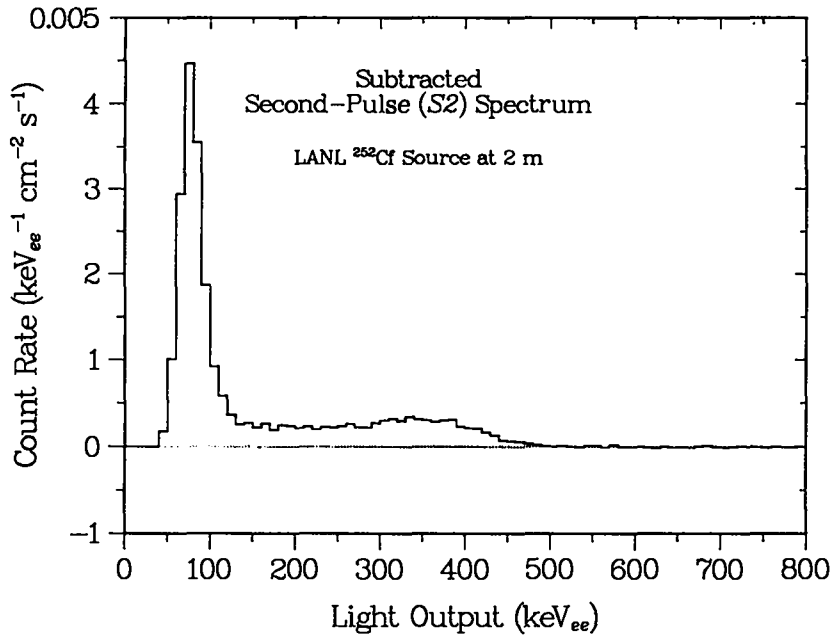

Fig. 2.3b. Corrected second-pulse (*S2*) spectrum resulting from the subtraction of the two spectra in Fig. 2.3a. The spectrum has a definite structure that is characteristic of the $^{10}B(n,\alpha)^{7}Li$ reaction.

neutrons, and cosmic rays—are eliminated by the subtraction of accidental coincidences. The remaining neutron background is estimated to be only about 0.003 $n \cdot cm^{-2} \cdot s^{-1}$. Thus, the detector is capable of providing extremely low background measurements of the fast-neutron count rate, an important issue for the APRF tests at long ranges.

Energy Measurements. The instrument's third and most important feature is its capability for determining the energy of each incident neutron, at least over the range of energies most important for fission sources, roughly 0.5–10 MeV.[7,9] Because obtaining the *S2* capture signature ensures that the neutron has slowed down and lost essentially all its energy, the light output from the first scintillator pulse (*S1*) must be related to the incident neutron energy. Two conversions are required. We first shift the observed light-output value to account for the nonlinear saturation in the energy-to-light conversion in the scintillator, which changes the electron-energy scale to one for neutron energy in MeV.[7,9] Because this "effective" energy-to-light conversion includes multiple scattering in the scintillator, we use a composite function[7] instead of a standard single-scattering parameterization.[18] Next, this spectrum is incremented according to the energy-dependent neutron-detection efficiency, which results in an absolute flux distribution dN/dE as a function of neutron energy. For the analyses in this report, results using both measured[7] and calculated[9] efficiency functions are included.

***S1* Difference Spectra.** The conversions for saturation and efficiency are appropriate only if all events in the spectrum are truly associated with absorbed neutrons. As with the *S2* spectra, nonneutron contributions are removed by subtracting the *S1* spectrum for events whose *S2* pulses fall in the late window from the *S1* spectrum for events with *S2* pulses in the early window. **Figure 2.5a** shows the two unsubtracted *S1* spectra, plotted as counts versus energy; these spectra use only the two rods facing the neutron source. The late window contains only accidental coincidences; the early window contains both true and

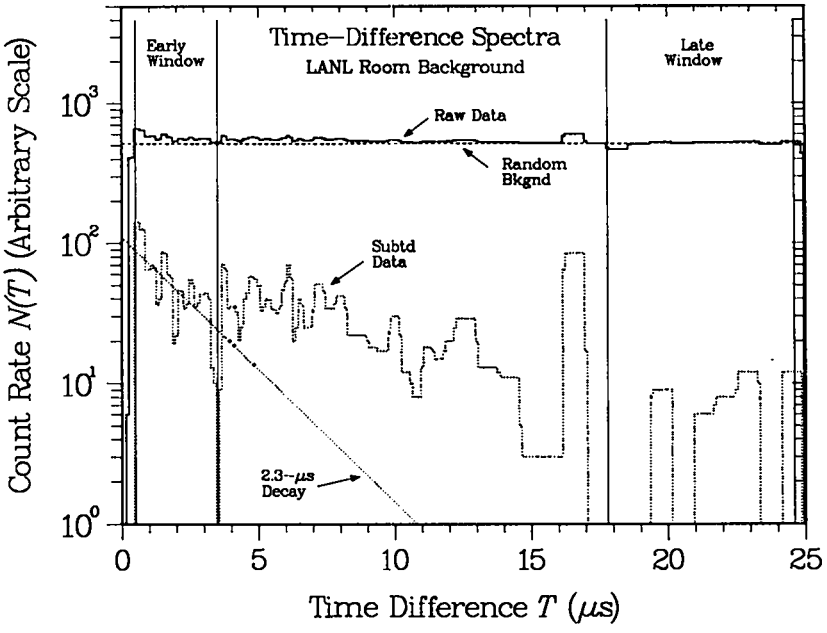

Fig. 2.4a. Time-difference spectra for measurements of the room background at LANL. When compared with Fig. 2.2, this figure shows a large random background and only a very small fast-neutron component.

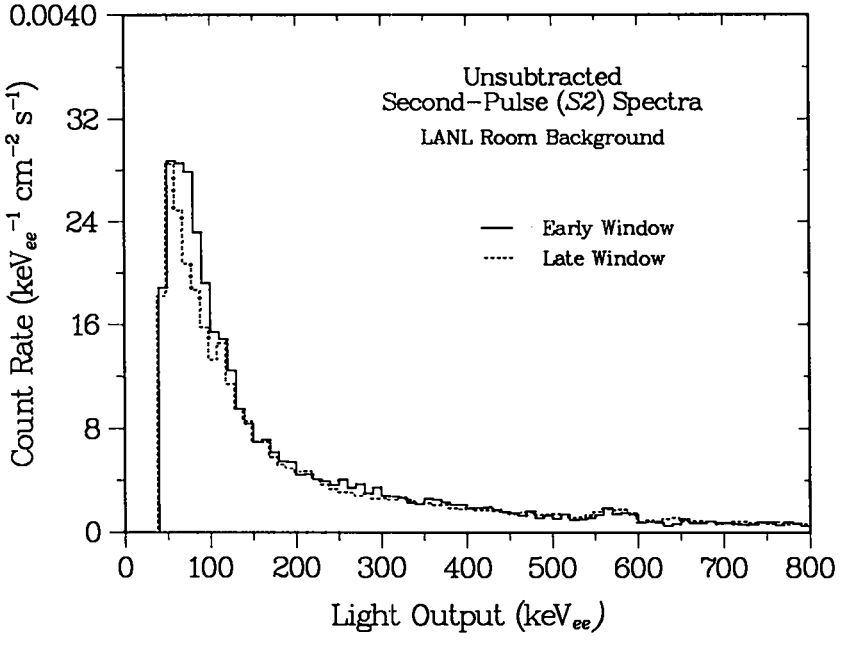

Fig. 2.4b. Unsubtracted second-pulse *(S2)* spectra for room-background events in the early and late windows of Fig. 2.4a. The slight difference between the two spectra indicates the small amount of neutron background.

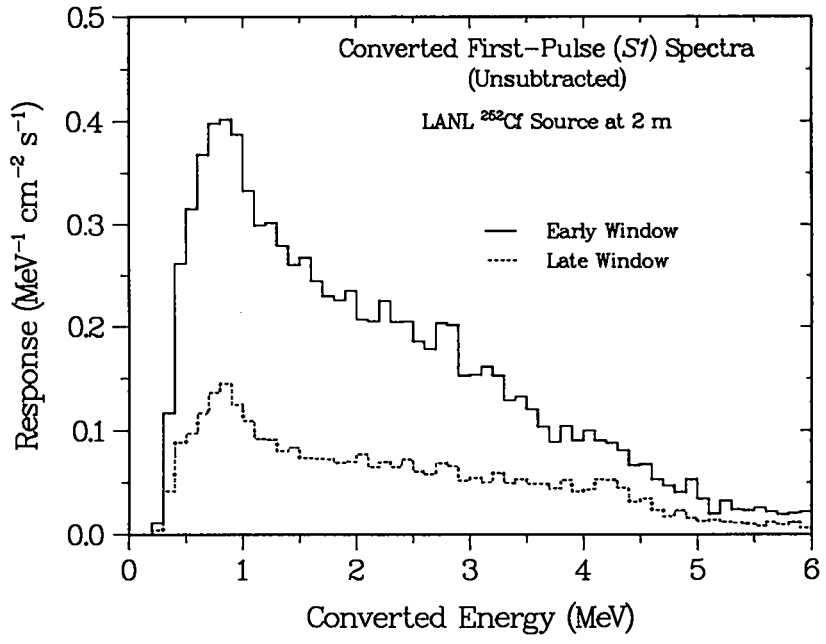

(a)

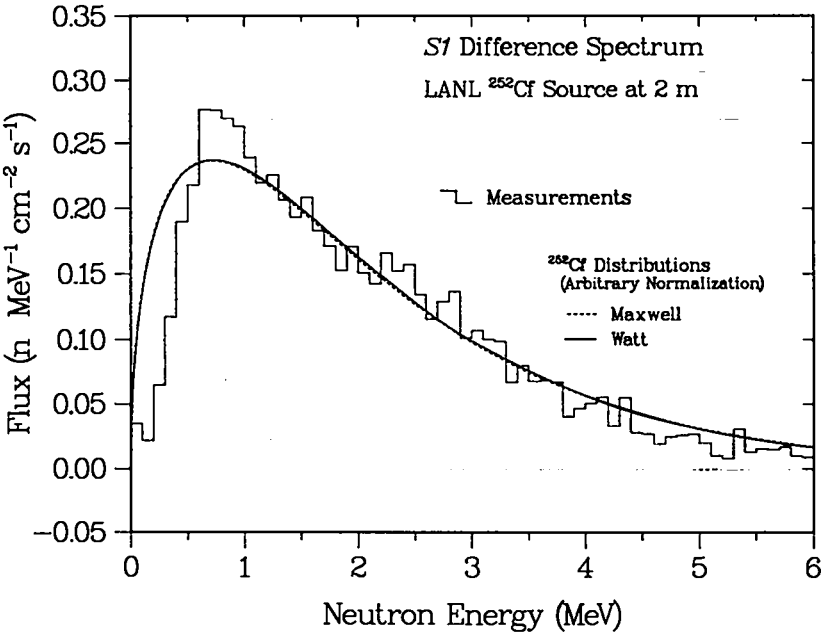

(b)

Figs. 2.5a,b. Part a: Energy spectra from the first pulses (*S1*) corresponding to *S2* pulses in the early and late windows. Part b: Difference spectrum from the subtraction of the two spectra in part a. The smooth curves show the energy dependence expected for a ^{252}Cf source, using an arbitrary normalization to match the data.

accidental coincidences. The most conspicuous feature in the accidental spectrum is the broad peak near 0.8 MeV, which is the converted analog of the 93-keV$_{ee}$ capture peak in the *S2* spectrum. The subtracted result, which can now be legitimately plotted as neutron flux versus neutron energy, is given in **Fig. 2.5b**. Shown normalized to the data are two ^{252}Cf distributions based on Maxwell and Watt functions,[19] which are equivalent for our purposes. The comparison shows the detector's minimum cutoff energy of about 0.5 MeV, which results from saturation in the scintillator's energy-to-light conversion; lower-energy proton recoils produce light-output pulses below the detector's electronic threshold, which is set at 40–50 keV$_{ee}$. Otherwise, the subtracted *S1* spectrum appears to follow the ^{252}Cf distribution rather well, although there seems to be a consistent deviation at the highest energies. We will return to this comparison in the next section.

Directionality. Just as the boron added to the BC454 scintillator provides the detector's unique energy-measurement capability, its multielement segmentation provides an unusual ability to indicate the average direction of the incident neutron flux. As discussed in previous reports on multielement neutron detectors,[16,17,20] attenuation across the detector and differences in solid angle result in differences in the count rates for individual rods. For simplicity, the characteristics of the directional flux and the resulting detector response can be described using the formalism of *polarized* radiation fields and detector *analyzing powers*. Briefly, a completely directional field would have a polarization $P = 1.0$; a completely random one would have $P = 0.0$. Similarly, a perfect detector would have an analyzing power $A = 1.0$, and a completely insensitive one would have $A = 0.0$. Taken together, a measurement of the polarization P using a detector with analyzing power A yields a count-rate asymmetry $P \times A$. In our case, this asymmetry is calculated from the difference between the count rates for elements on opposite sides of the detector.[17] For example, in the calibrations the source was placed in front of the detector, with two rods facing the source and two on the rear side. In this arrangement the front/back ratio between the count rates was about 4:1. In contrast, for the reactor runs at APRF, this ratio was only 1.5–1.8 to 1, which immediately indicates a much more isotropic angular distribution, that is, a lower polarization. This discussion—in terms of both polarization magnitudes and directions—introduces the detector's fourth important feature, directional capability, which will be discussed in detail in Sec. 3 using the APRF measurements.

Discussion. This section has explained at some length the important aspects of the unique neutron instrument used for these measurements. The first feature is the use of a specific signature that selects only fast neutrons and eliminates all other background sources. This selectivity relies on a simple recoil-and-capture mechanism that leads to an exponential time-difference spectrum and a characteristic second-pulse capture distribution, which in turn provides an internal pulse-height calibration, the detector's second important feature. The enforcement of these selection criteria leads to the subtraction of measurements for true and accidental coincidences, which is important for the detector's third feature, the direct production of the energy distribution of the incident neutrons without any unfolding. Finally, the fourth feature of the detector, its segmentation, can be used to indicate the magnitude and direction of the polarization in the incident neutron flux, which will be useful in interpreting the measurements at APRF. All four features have been discussed in terms of measurements with a laboratory ^{252}Cf source, which provide the basis for calibrating the magnitude and shape of the detector response, as discussed in the next section.

3. APRF CALIBRATIONS AND MEASUREMENTS

Introduction. The APRF dosimetry study consists of two parts, reliability tests and reactor spectra. As discussed in the previous section, the detector provides several features that help to ensure the integrity of the data, and reference measurements using ^{252}Cf sources provide valuable end-to-end checks under conditions similar to the reactor measurements. This systematic approach will be emphasized in the discussion presented here.

^{252}Cf Calibrations. The value of the ^{252}Cf source tests is illustrated by the continued analysis of the measurements in Fig. 2.5b. **Figure 3.1a** repeats the 2-m results and shows additional data at a 1-m separation, divided by 4 to correct for the difference in solid angle. To test the reliability of the data analysis, we used several different approaches, all of which should give consistent results. One choice is the use of either measured efficiencies[7] or calculated values that have been modified by a high-energy tail correction;[8] both options are supported by previous analyses.[9] Another choice is the use of spectra from all four rods, both front and back, or from only the two rods that face the source. Because of the partial attenuation of the neutron flux as it passes through the detector, the two-rod choice provides a slightly better signal-to-background ratio,[16,17] but using four rods increases the detector's overall efficiency by about 30%.[9] As hoped, all four combinations give almost identical results, so the values in the figure are an average with uncertainties that include the deviations between the different analyses.

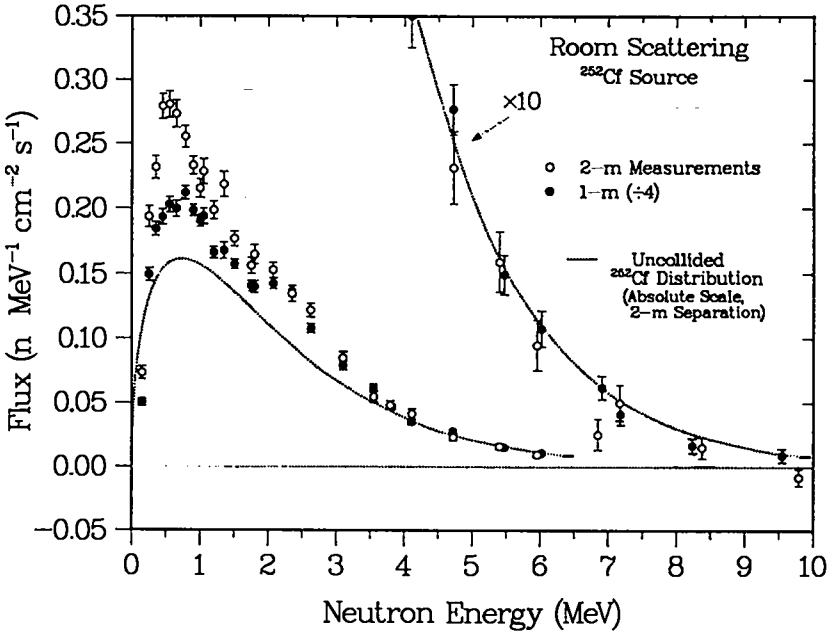

Fig. 3.1a. Neutron energy spectra for ^{252}Cf sources at distances of 2 m and 1 m, scaled by $1/r^2$ to compensate for the difference in solid angle. The ^{252}Cf distribution is calculated for a 2-m separation using the calibrated source strength.[21]

Room Scattering. The comparison between the two measurements in Fig. 3.1a, particularly regarding the increase in the scaled count rate with increasing distance, suggests a problem with room-return backgrounds. This suggestion is strongly supported by the comparison with the expected ^{252}Cf distribution, which is normalized to give an energy-integrated flux of 0.48 n·cm^{-2}·s^{-1} at a 2-m separation, based on the calibrated source strength of 2.4×10^5 n·s^{-1} (±2%).[21] Ideally, one could eliminate the room-scattering effect by subtracting two measurements, one made with a thick "shadow bar" placed between the source and detector.[22] Because this arrangement is physically awkward for a large detector, we have used an alternate approach of comparing measurements with computer simulations. In **Fig. 3.1b** we show the 1-m and 2-m measurements along with Monte Carlo calculations using the LANL Monte Carlo N-Particle (MCNP) radiation-transport code.[23] It is immediately apparent that the measurements are in excellent agreement with the calculated MCNP fluxes at both separations—that is, the apparent discrepancy in Fig. 3.1a is simply a matter of neglecting the room-scattered neutrons, which produce the 50% difference between the measurements and the uncollided flux. Other calculations indicate that the size of this contribution is largely determined by the floor return, and the definite structure near 2 MeV is a room/air crosstalk effect that appears only with the inclusion of air scattering. The enlarged view at high energies shows that the good agreement between the measurements and calculations extends to energies of at least 10 MeV. In short, with the recognition of the 50% contribution from room scattering, the measurements and calculations are entirely consistent. This comparison establishes the absolute normalization used for all the APRF measurements, which we can assume to be accurate to within about 20% from 0.5 to 1.0 MeV, 10% from 1 to 4 MeV, and about 30–50% from 4 to 10 MeV.

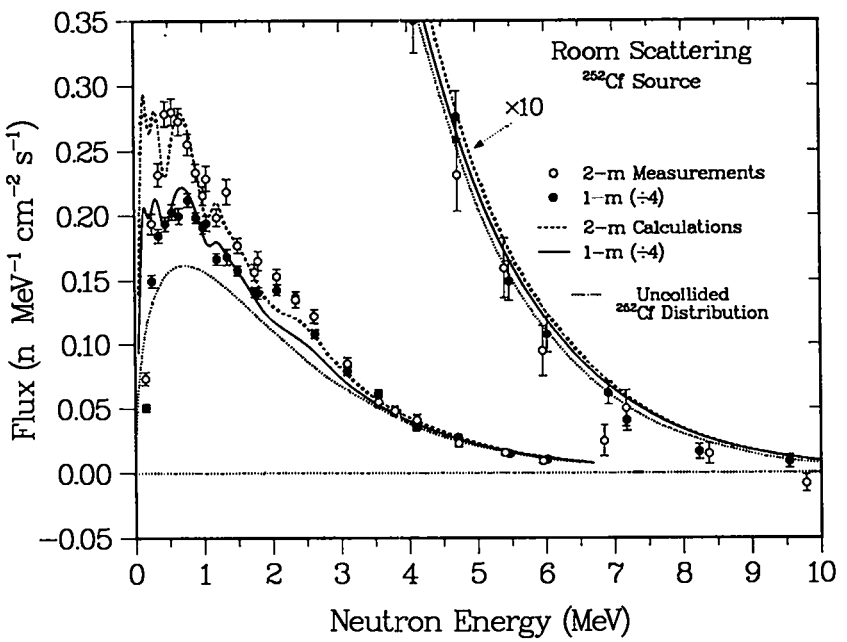

Fig. 3.1b. Neutron energy spectra for ^{252}Cf sources at distances of 2 m and 1 m, compared with Monte Carlo calculations that include the effect of room-scattered neutrons. The agreement at both distances is excellent.

Indoor ^{252}Cf Calibration. Upon arriving at APRF, we repeated the 2-m measurements made indoors at LANL, this time using an APRF ^{252}Cf source. In these tests neither the time-difference spectrum, the *S2* capture spectrum, nor the *S1* energy spectrum showed any systematic differences from the calibrations at LANL. The measured ratio of 4.8 between the APRF and LANL measurements agrees within 15% with the ratio of 4.2 between the reported source strengths of 1×10^6 n·s^{-1} (APRF) and 0.24×10^6 n·s^{-1} (LANL). Given the likelihood of differences in the room scattering at the two locations, this agreement is quite reasonable.

Field Calibrations. The largest distance used at APRF was 1620 m from the reactor. With the reactor off, the singles background rate was a factor of about 4.5 lower than the rate measured indoors at LANL, and the subtracted *S2* spectrum, which includes only fast neutrons, was lower by about 30%. The singles difference is probably an effect of the indoor/outdoor ratio of gamma-ray fluxes, and the smaller fast-neutron flux may be associated with different cosmic-ray backgrounds at the two altitudes. The detector was also checked by measuring a spectrum for the LANL ^{252}Cf source (shipped to APRF). This calibration happened to be made with the source 2 m from a corner rod, not a detector face, which allowed a test of the four-rod and one-rod efficiencies developed in Ref. 9, again with excellent agreement. **Figure 3.1c** shows the comparison between the ^{252}Cf calibration and MCNP calculations that include the effect of air and ground scattering. The two curves are for dry soil and soil with 25% by weight of added water, the value estimated for APRF.[24] Other calculations using water contents between 10% and 40% show a systematic variation, with the best agreement obtained for values between 20% and 30%. The indoor calibrations with the APRF ^{252}Cf source were our first measurements made at APRF, and the field calibrations with the LANL source were the last. These two calibrations bracket the reactor data in time, thereby providing an effective guarantee of the measurements' reliability.

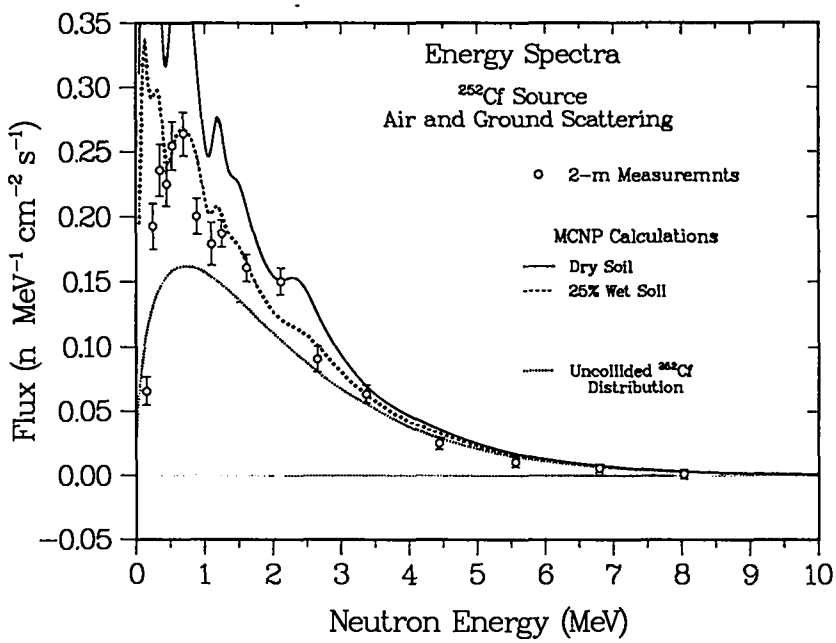

Fig. 3.1c. Neutron energy spectrum for a ^{252}Cf source at a distance of 2 m compared with Monte Carlo calculations that include scattering from soil with different water contents. The agreement is excellent for the calculations with a 25% water content, the estimated APRF value.

Measurement Scenarios. The first reactor data were taken for the 1080-m location at a height of 155 cm above the top of a small hill, whose crest was about 12 m above the surrounding area. With the reactor located about 14 m above ground level, the line of sight to the source passed just below the level of the tree line. (For plan and elevation layouts of the site, see the diagrams in Ref. 25.) Because of a high detector counting rate apparently associated with low-energy neutrons, the reactor power level was reduced to 1 kW to allow a single 576-s run. Even at this lower power level, the count rates still cause some concern about the detector's dead-time correction. In contrast, for the following 4416-s measurement at 1620 m, there were no dead-time difficulties even with the reactor running at the usual 8-kW level. **Figure 3.2** shows the resulting 1620-m time-difference spectra. Although the random background is now much higher than for the calibrations with the LANL ^{252}Cf source (Fig. 2.2), the rates are still lower by about 30% than those for the successful calibrations with the APRF source. **Figure 3.3** shows the subtracted *S2* spectrum for this distance, which confirms the neutron identification and the accuracies of the accidental subtraction and gain calibration. In particular, the comparison with the subtracted spectrum for the LANL ^{252}Cf source (Fig. 2.3b) shows that both shapes are exactly the same.

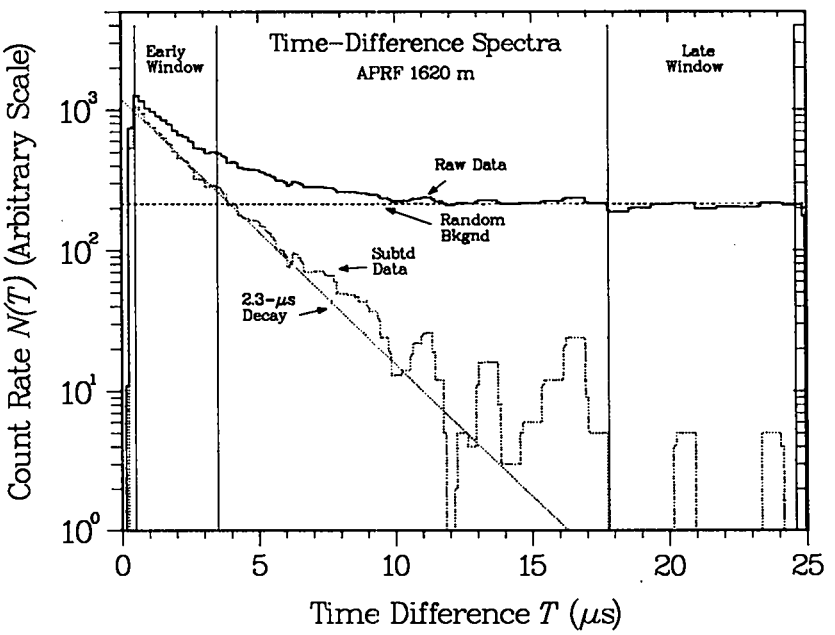

Fig. 3.2. Time-difference spectra for the 1620-m APRF measurements with the reactor operating at 8 kW. The behavior is qualitatively the same as for the calibration run with the ^{252}Cf source (Fig. 2.2).

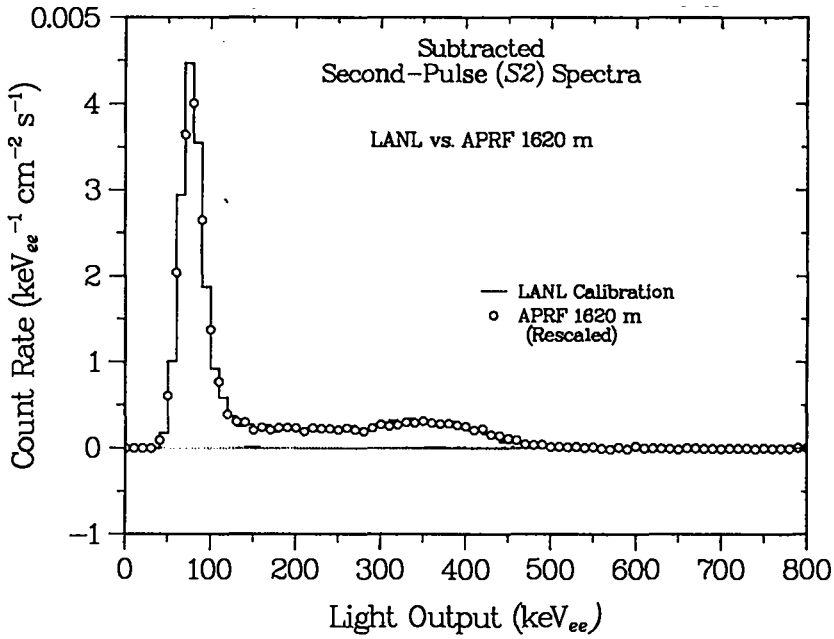

Fig. 3.3. Subtracted *S2* spectrum for the 8-kW reactor run at the APRF 1620-m position, compared with that for the ^{252}Cf calibration run.

The 1080-m Energy Distributions. As with the source calibrations, the reactor measurements were converted to neutron fluxes using both measured[7] and calculated[9] corrections. Because the detector's directionality indicated a relatively small difference between the count rates for the four rods (discussed below), only four-rod values for the efficiency were used. **Figure 3.4a** shows the resulting 1080-m energy spectrum as a function of differential energy (d/dE), using either the full detector resolution (fine) or rebinning the results (coarse) to improve the statistics. (The coarse-resolution data for both the 1080-m and 1620-m distances are included in **Appendix A.**) The data are normalized using the reactor power in kW (1.0 kW at 1080 m), the measurement time in hours (576 s = 0.16 h), and the flight path in meters (1080 m). The number of source neutrons per kWh was taken as 1.28×10^{17} (Ref. 6). The error bars show the statistical uncertainties only, not the estimated systematic errors.

Comparison with Other Data. **Figure 3.4b** plots the BC454 coarse-resolution data along with measurements that represent the two other important spectroscopic techniques, recoil-scintillator (NE213) data[6,26] from the Defence Research Establishment, Ottawa (DREO), and three separate measurements with a set of polyethylene-moderated neutron-capture detectors (a "Multisphere" spectrometer).[27] We stress that the Multisphere results presented here are from a preliminary analysis of the first of two sets of measurements made by the Environmental Measurements Laboratory (EML) of the Department of Energy (DOE). (The preliminary spectral unfolding used old detector response functions calculated from now-obsolete cross sections, and EML is currently reanalyzing all its data using new response functions.) The variation in distance from 1070 to 1080 m for the different measurements should have little effect, especially with each measurement normalized by the square of the distance R. In general, the agreement between the techniques is quite good, apparently consistent within the ±30% value implied by the corresponding spectral

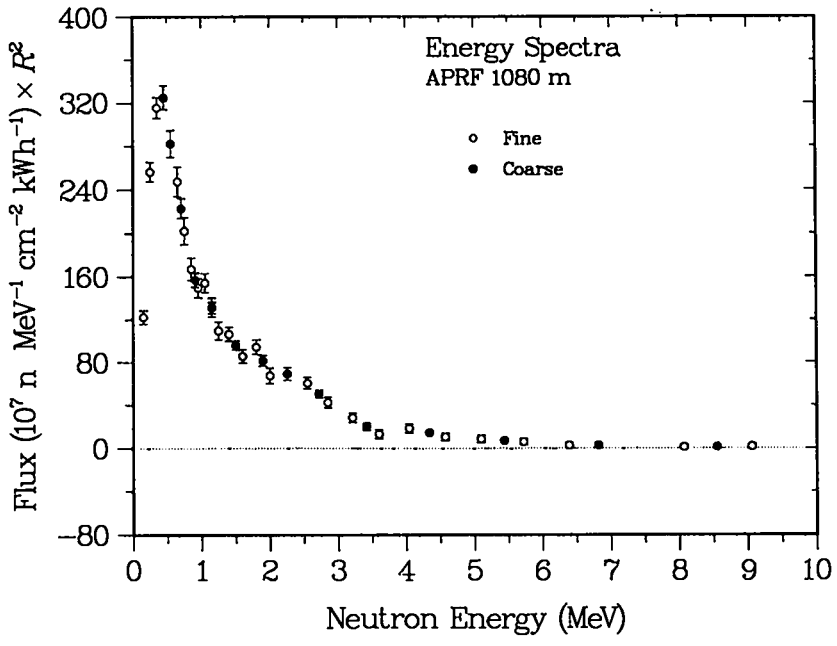

(a)

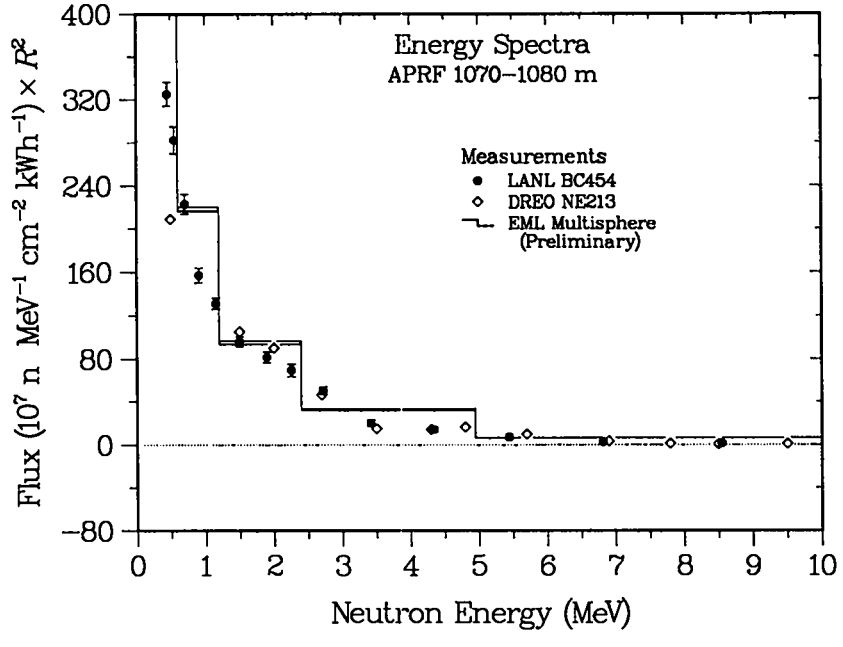

(b)

Figs. 3.4a,b. Neutron energy spectra for the 1080-m APRF measurements. Part a shows the full-resolution and rebinned results from the present work; part b compares the rebinned data with results from two other measurement techniques.

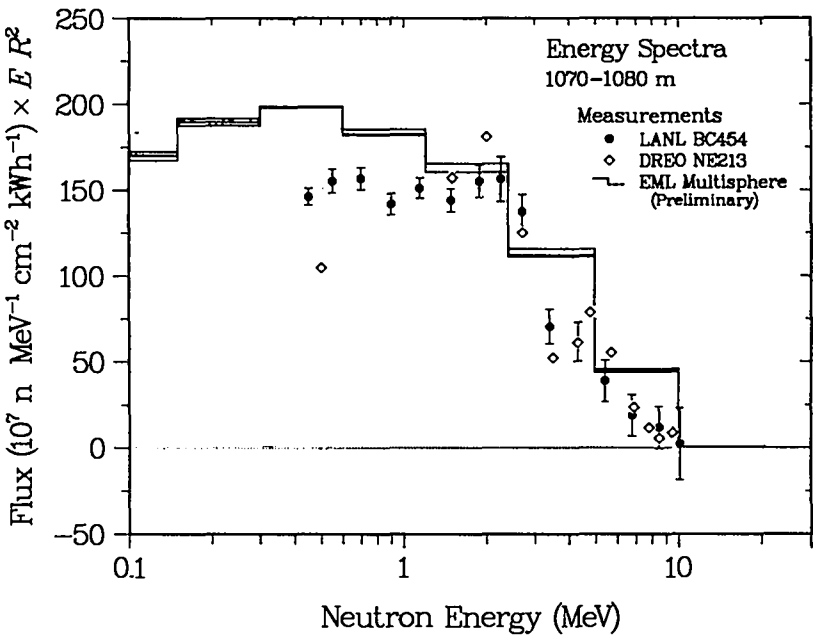

Fig. 3.4c. Comparisons between measurements at 1080 m, with the differential-energy data in Figs. 3.4a,b replotted in terms of differential lethargy multiplied by the square of the distance R.

comparisons in Ref. 6. To allow closer inspection, in **Fig. 3.4c** we replot the measurements in terms of differential lethargy (that is, $d/d\ln E = Ed/dE$), which gives an energy-weighted differential flux that is more appropriate for display on a logarithmic energy scale. Again, the present results are in excellent agreement with the similar scintillator results from Ref. 26, both in magnitude and structure. (The low DREO data point at 0.5 MeV is probably a threshold effect.) Near 2 MeV, the agreement with the preliminary Multisphere data provides an independent check on our overall normalization. At energies below 1 MeV, the BC454 data are prone to threshold effects; at higher energies, the preliminary Multisphere data are systematically 30–50% higher than the two scintillator measurements. Taken as a whole, however, the combined data set appears to establish the reactor flux to within ±20% accuracy.

The 1620-m Reactor Spectra. At the reduced count rates of the 1620-m location, two sets of measurements were made at 8 kW for a total duration of 1.23 h. **Figure 3.5a** shows the full-resolution and rebinned data, along with three sets of preliminary Multisphere results. (The differences between the Multisphere spectra are probably caused by rapidly changing weather conditions over the duration of those measurements.[27]) **Figure 3.5b** again replots the measurements in differential-lethargy form to allow closer inspection. The comparison between the two experimental techniques shows almost the same pattern as at the shorter distance, with the preliminary Multisphere results generally 20–50% higher than the present data.

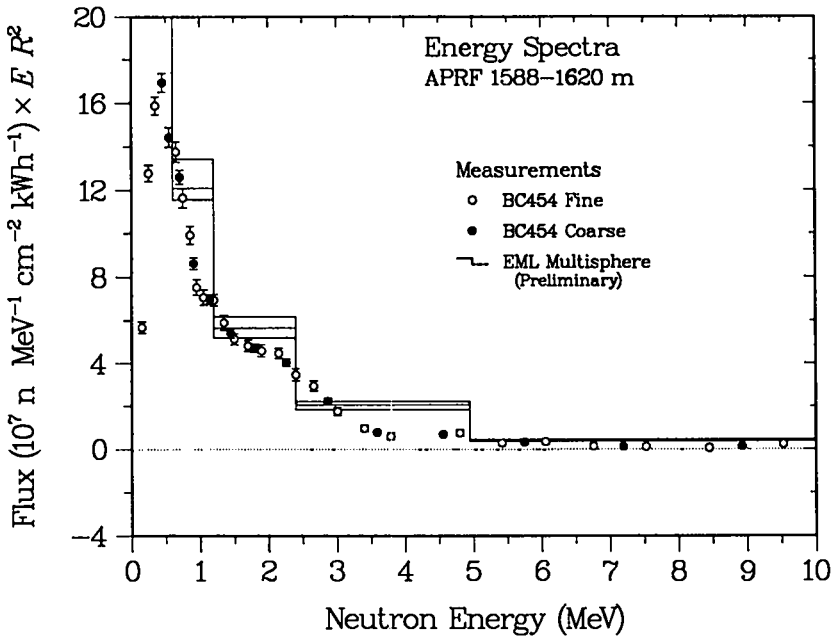

(a)

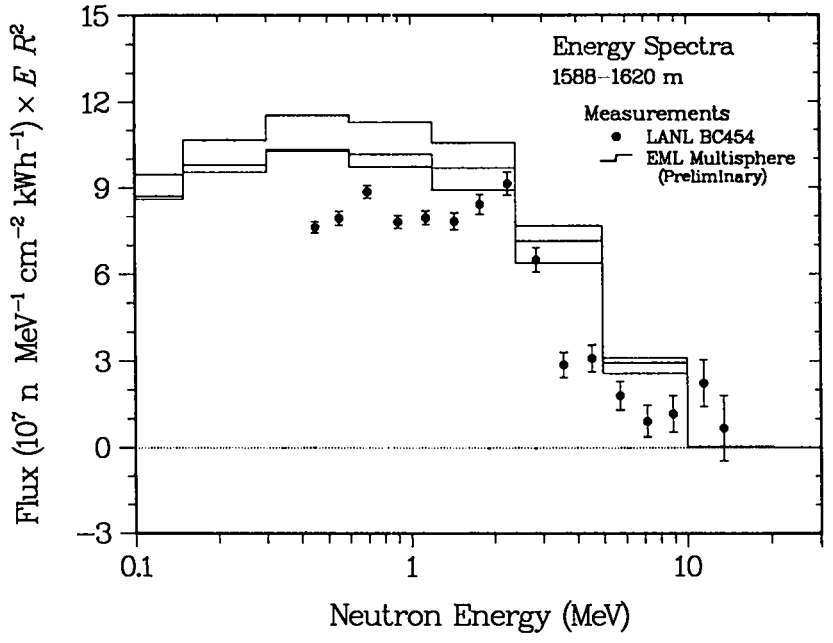

(b)

Figs. 3.5a,b. Neutron energy spectra at 1588–1620 m. Part a compares the measurements in terms of differential-energy (d/dE) distributions; part b shows a logarithmic energy plot ($d/d\ln E$).

Differential Dose Dependence. For comparison with other APRF data, it is useful to relate our energy spectra to integral dose measurements. The first step is to convert the differential-lethargy spectra (Figs. 3.4c and 3.5b) into differential dose values using energy-dependent fluence-to-dose functions.[24] This form of display makes it easy to visualize the contribution of different energies to the integral dose. **Figures 3.6a,b** show the 1080-m and 1620-m results corresponding to the flux spectra in Figs. 3.4c and 3.5b. As expected, the Multisphere data are larger by as much as a factor of 2 at higher energies. The real point in the figures, however, is the rapid falloff in the differential dose at lower energies. Although our measurements cover only a small portion of the logarithmic energy range, this portion accounts for a sizable fraction of the total dose.

Integral Doses. To arrive at a value for the energy-integrated dose, it is necessary to estimate the contribution from the part of the spectrum below 0.5 MeV. Although the dose functions in Figs. 3.6a,b decrease rapidly toward low energies, there are many decades of response that must be included in the integral. One approach follows the prescription introduced by Kazi et al., who assumed a low-energy differential-energy flux varying as $1/E$, which results in a constant differential-lethargy spectrum, as is generally observed.[6] Adding such an extension to our fast-neutron spectrum allows us to estimate the total dose, with the result that about 50% appears to be associated with energies below 0.5 MeV. Alternatively, we can simply add our high-energy dose to the integrated low-energy Multisphere data. If we use the first approach, our spectra extrapolate to estimated total doses ($\times R^2$) of 18.2±0.7 cGy·kWh^{-1}×m^2 at 1080 m and 1.04±0.04 cGy·kWh^{-1}×m^2 at 1620 m. The alternative approach of using the low-energy Multisphere integrals gives corresponding values of 14.9 and 0.83 cGy·kWh^{-1}×m^2. If we discount the preliminary Multisphere data at high energies, we can expect integral doses of 16.5 and 0.9 cGy·kWh^{-1}×m^2 at the 1080-m and 1620-m distances, with an apparent variation of about ±10%. These values are completely consistent with the recent Rem-meter measurements reported by Heimbach et al.,[25] which give 17.0 and 0.87 cGy·kWh^{-1}×m^2 at the 1080-m and 1600-m distances.

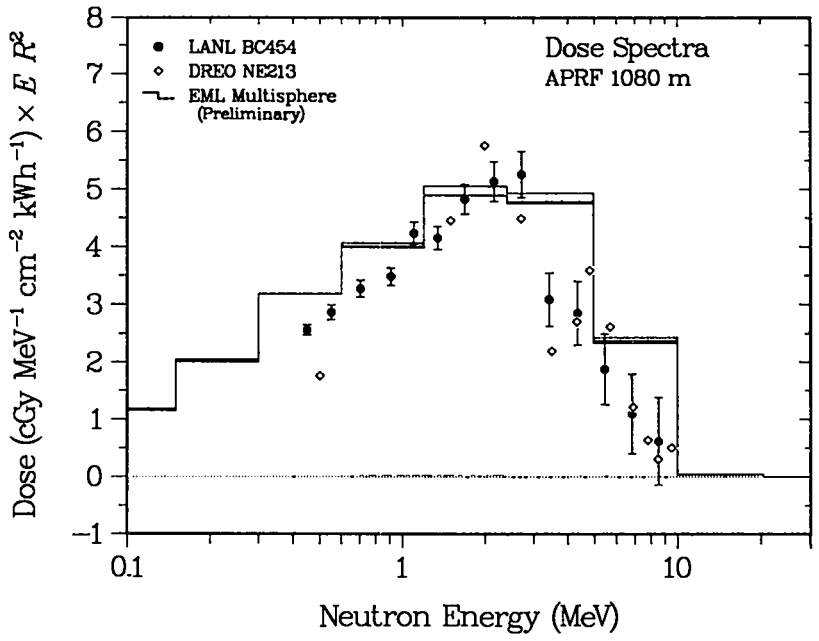

(a)

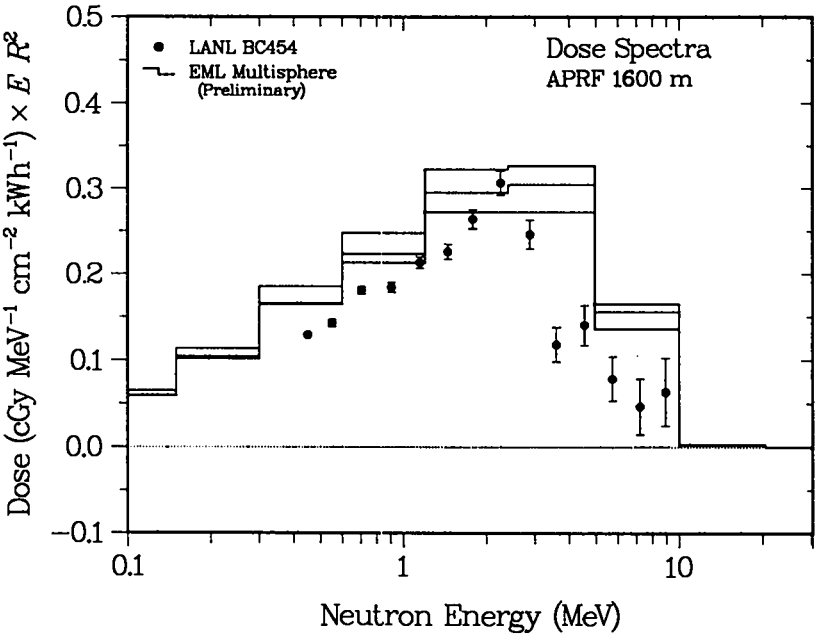

(b)

Figs. 3.6a,b. Differential neutron-dose distributions at 1070–1080 m (part a) and 1588–1620 m (part b).

Directionality. We close this section with a discussion of the additional information about the long-range APRF neutron field revealed by the use of our multielement detector. We first return to the ^{252}Cf calibrations made at LANL and at the 1620-m location at APRF. **Figure 3.7** illustrates these measurements schematically, with the horizontal axis of the four-rod detector viewed end-on. The 1-m and 2-m calibrations at LANL were made with the source facing a pair of rods (at 0°), but the calibration at the 1620-m location was made with the source placed 2 m diagonally downward from a corner rod; the combined results therefore provide a check on our calculations about the detector's directionality. In the figure, the open circles show the actual source locations, the directions of the vectors show the angles observed at the detector, and the lengths of the vectors are the observed polarization magnitudes. The calculations are shown as dashed vectors; the measurements use solid vectors and arc lengths that indicate the statistical uncertainty. At LANL, the indicated source directions (with statistical uncertainties) are $\theta = -4 \pm 1°$ at 1 m and $\theta = -2 \pm 2°$ at 2 m, with the negative values indicating a slightly downward offset, a possible result of floor scattering. Previous angular studies of our unshielded four-rod detector suggest that the systematic angle accuracies are of the order of $\pm 5°$ (Ref. 17). The corresponding values from simple MCNP calculations are $\theta = -4°$ at 1 m and $\theta = -6°$ at 2 m, in fair agreement. Accordingly, the APRF calibration should show a downward rotation of $-45°$: the measured value is $\theta = -51 \pm 4°$, the calculated one is $-41°$, again in reasonable agreement. For the estimated polarizations, the measured value for the source calibrations is $P = 0.93 \pm 0.10$; the calculated value is 1.0. For the reactor runs (assuming the same detector analyzing power as for the calibrations, that is, a similar energy spectrum), the measured polarizations at both distances are consistent with $P = 0.36 \pm 0.04$, with an

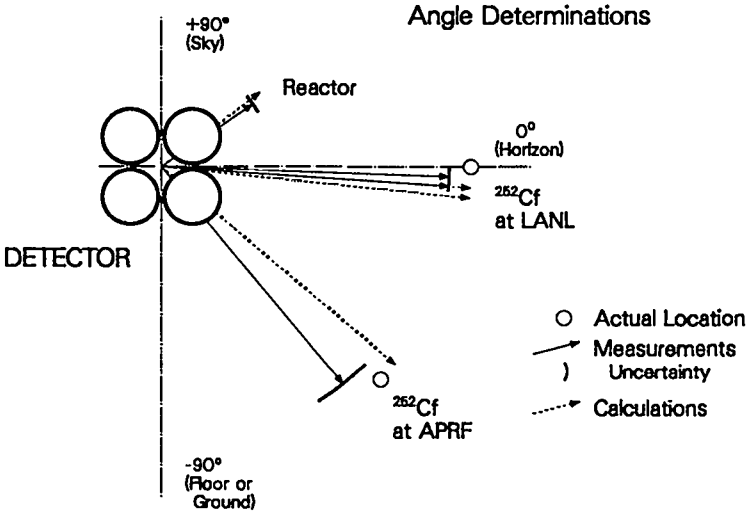

Fig. 3.7. Layout for directions observed using the four-rod detector with its axis horizontal. Vectors indicate measured and calculated angles as seen from the detector; open circles indicate the actual directions.

apparent source angle oriented upward toward the reactor at about $\theta = 35 \pm 5°$ above the horizon. The calculated values are $P = 0.40 \pm 0.02$ and $\theta = 37 \pm 2°$, in very good agreement. These results are consistent with a picture in which skyshine, not direct transmission, is the dominant radiation source at large ranges.

Discussion. Four observations stand out in the APRF preparations and field measurements. First, the source calibrations, both at LANL and at APRF, ensure the reliability of the data in the 0.5- to 10-MeV range, at least within the detector's 10–30% normalization uncertainty and 20–40% energy resolution. Within the collective uncertainties for the reactor data, at both distances there is fair-to-excellent agreement among spectral measurements obtained using different techniques. Second, although there may be concerns about the 30–50% discrepancies with the preliminary Multisphere data at high energies, the overall extrapolation to integral doses still gives estimates that are consistent within 10% with recent Rem-meter measurements. Third, the reactor spectra are nonexponential in shape and include clear evidence of air/ground scattering. Fourth, the multielement analysis indicates that about 30–40% of the incident flux is incident downward at an angle of about 35°, in agreement with simple calculations. This result strongly suggests a picture in which skyshine combines with direct transmission to produce a complex radiation field at large ranges. These last two points will be pursued further in the next section.

4. COMPARISON WITH CALCULATIONS

Overview. We now examine some of the systematic behavior associated with fast-neutron transport at long ranges, which leads to our presentation of representative calculations for comparison with the measured spectra. We begin by relating the observed energy structure to features in the nitrogen and oxygen cross sections, and we conclude by demonstrating the generally satisfactory agreement obtainable between the measurements and full-scale calculations.

Direct Transmission. Because the neutrons must pass through a nitrogen/oxygen mixture, structure in the total cross section for either element can have a profound effect on the transmitted spectrum. Specifically, only if there exist overlapping cross-section minima (transmission maxima) for both elements can source neutrons reach the target directly. To indicate such transmission "windows" qualitatively, in **Fig. 4.1** we show calculated 1000-m transmissions for both nitrogen (dotted curve) and air (80% nitrogen, 20% oxygen; solid curve). Only where the nitrogen and oxygen cross sections overlap is there a window, such as at 2.3–2.9 MeV, at 4.8–5.1 MeV, and from 6 to 10 MeV. At 0.95 MeV, however, the peak in the nitrogen transmission does not coincide with one for oxygen, so there is no net transmission. In addition, the dashed histogram shows an MCNP result rescaled from a calculation at 1080 m for the direct (uncollided) transmission; the agreement with the simple cross-section calculation is satisfactory.

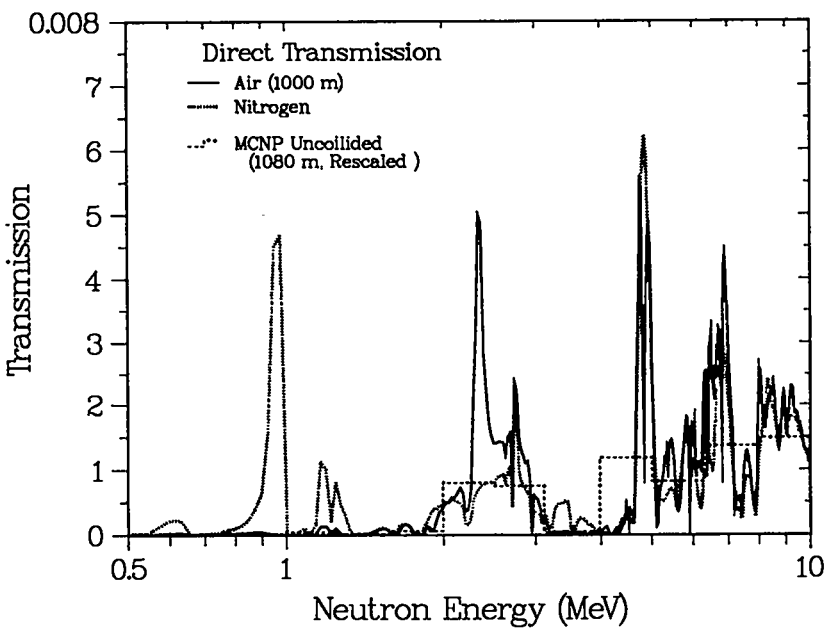

Fig. 4.1. Comparison between transmissions obtained from simple cross-section calculations and uncollided MCNP transport. No solid angles are included.

Total Transmissions. The direct or uncollided transmissions in Fig. 4.1 are of limited relevance in a deep-penetration problem such as the one studied in this report. A more useful quantity is the probability that a neutron that starts from the source at a given energy will reach the detector at any energy above the 0.5-MeV detector cutoff. **Figures 4.2a,b** show these total transmission functions for both distances, along with the corresponding direct transmission obtained from the uncollided MCNP tally. It is clear that the scattered contribution is much larger than the direct fluence and that the structure becomes more pronounced as the distance increases. This structure is largely washed out in the total transmission, however, because this quantity integrates over all energies at the detector. Comparison with our spectral measurements requires a transmission calculation that relates the energies at the source to those eventually observed at the detector, as discussed next.

Differential Source-to-Detector Transmissions. To correlate particular regions of the source and detector spectra, we can project out the energy spectrum at the detector from each of the source-energy bins shown in Figs. 4.2a,b. To simplify the results, we have expressed the detector contributions on the fractional basis shown in **Figs. 4.3a,b**. Here, the x-axis gives the energy observed at the detector, and the y-axis shows the cumulative fraction of the detector spectrum that originated from particular portions of the source spectrum, as indicated by the range labels in each band. As appropriate for the roughly exponential source spectrum, the source energy bins increase logarithmically; the percentage that each bin represents in the total source spectrum is given by the small italicized numbers. At the 1080-m distance (Fig. 4.3a), most (~60%) of the neutrons detected at 3 MeV come from the less than 4% of the source spectrum above 4 MeV. Similarly, only about 16% of the 0.5-MeV neutrons come from the 66% of the source neutrons in the lowest 0- to 1.3-MeV source band; the remaining 84% are downscattered from higher energies. In fact, because of the transmission window near 4.8 MeV, the 3-MeV neutrons are three times as likely to have come from the 4- to 6-MeV portion of the source spectrum as from the 3- to 4-MeV section, despite the equivalent source integrals. At 1620 m, this ratio increases to almost 9:1. This behavior emphasizes the relative importance of both transmission windows and the high-energy part of the source spectrum for detected neutrons at all energies.

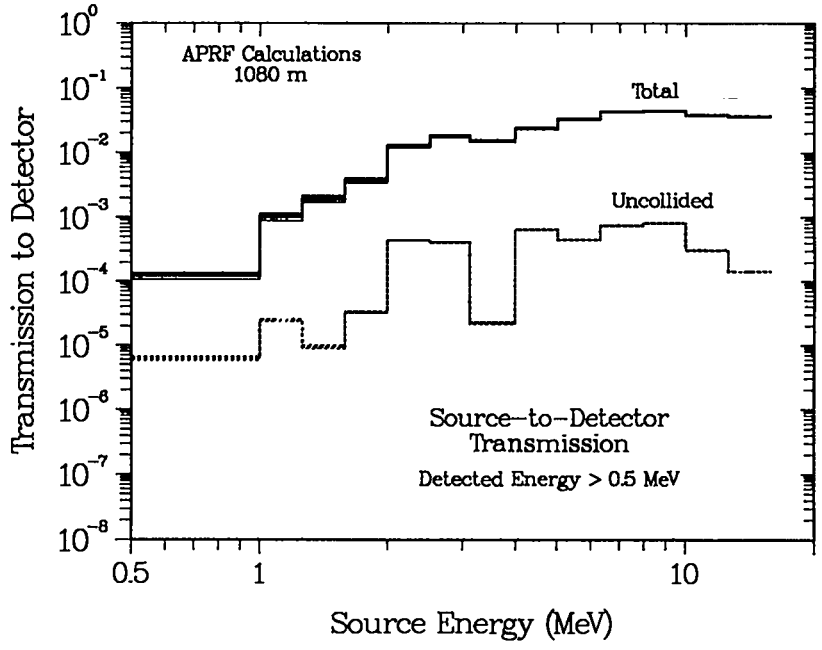

(a)

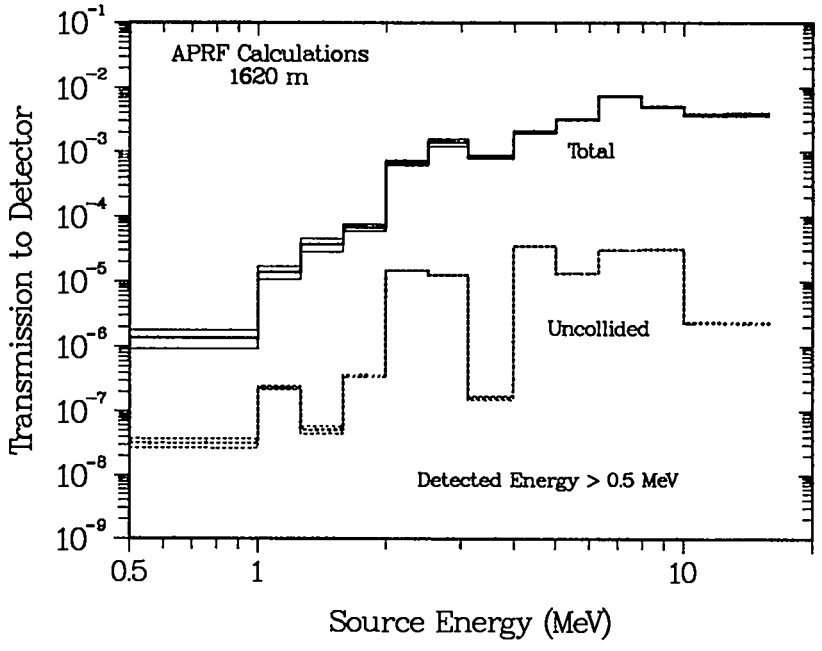

(b)

Figs. 4.2a,b. Total and uncollided transmissions as a function of energy at the source. Part a is for 1080 m; part b is for 1620 m. Neutrons below 0.5 MeV are not included.

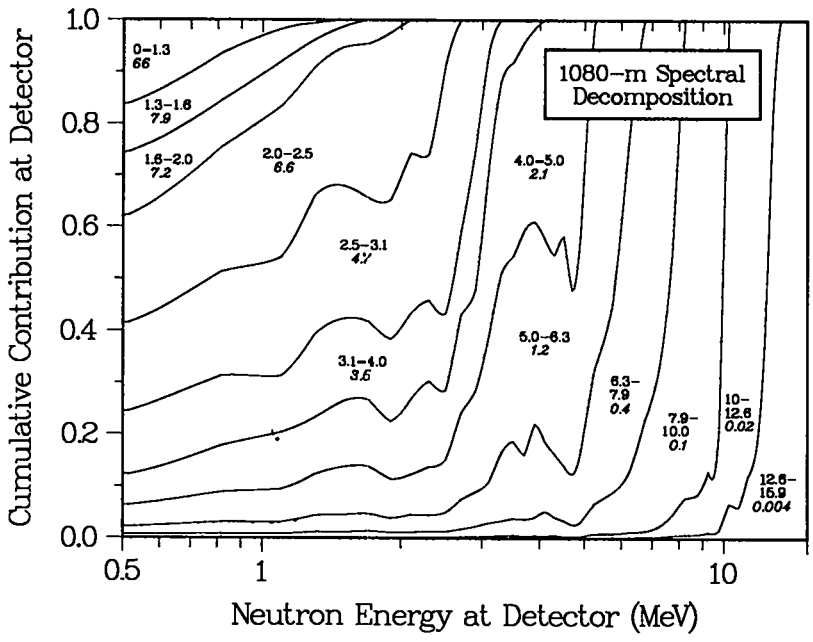

(a)

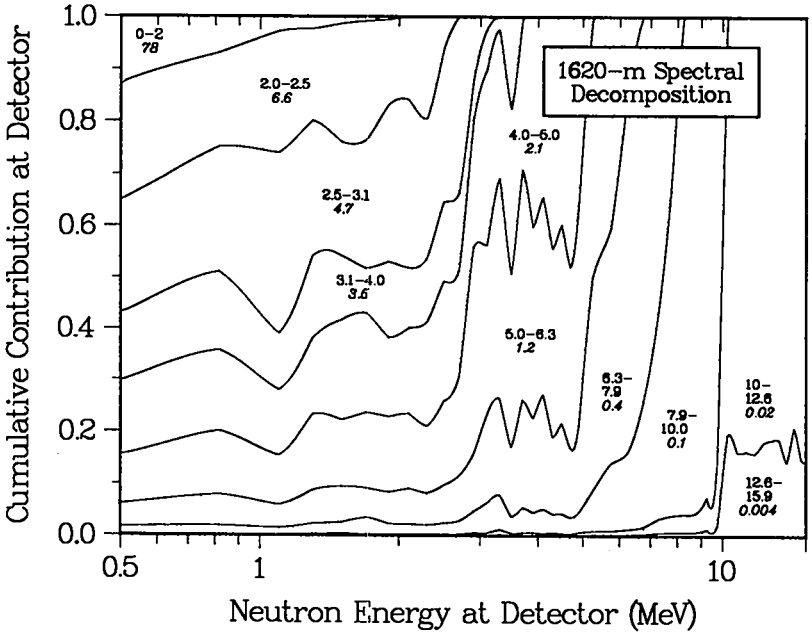

(b)

Figs. 4.3a,b. Fractional detector contributions from specific regions of the source spectrum. At each x-axis detector energy, the y-axis sections indicate the cumulative fraction of the detector response obtained by adding each portion of the source spectrum. The small numbers identify the source band, with the source percentage in italics. Neutrons below 0.5 MeV are excluded from the totals. Part a is for 1080 m; part b is for 1620 m.

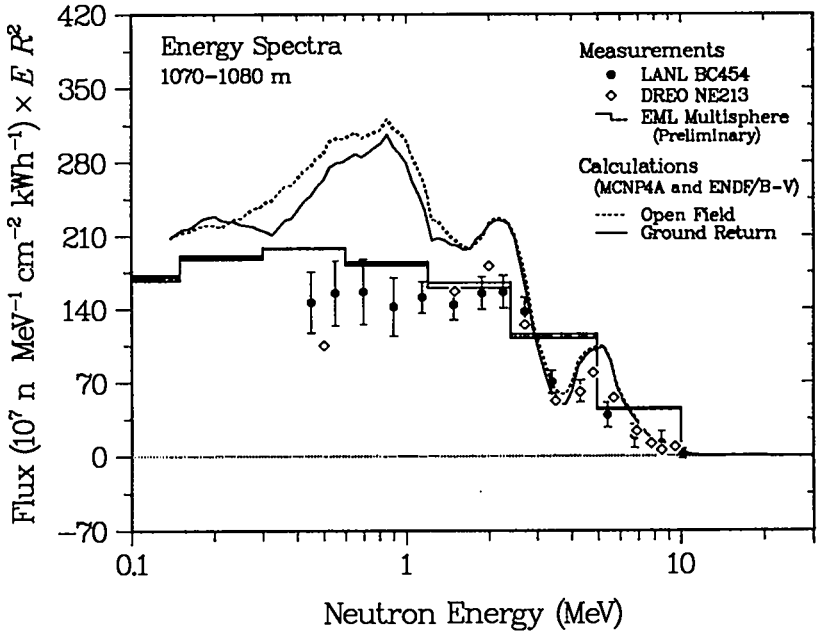

(a)

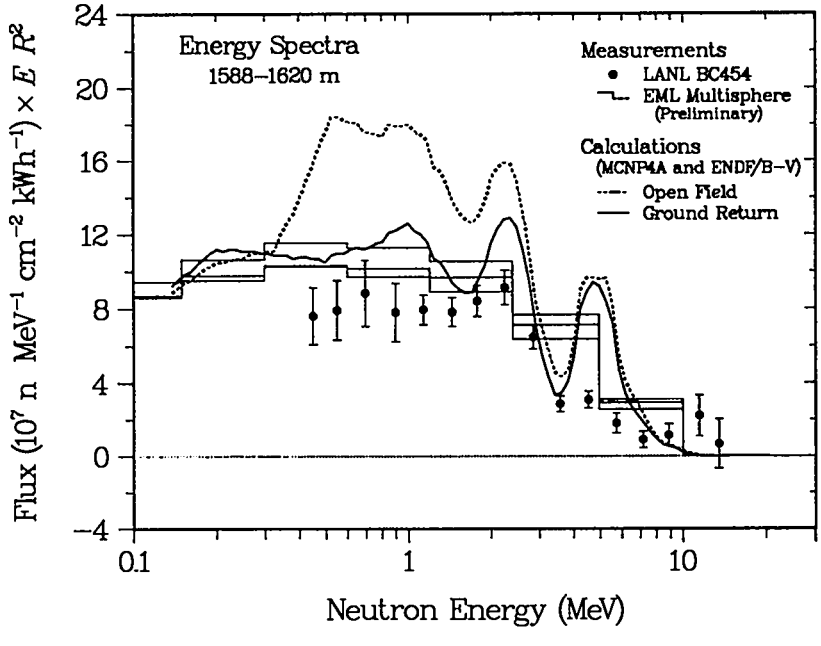

(b)

Figs. 4.4a,b. Comparisons between measurements and MCNP4A calculations, emphasizing the effect of ground scattering. Part a is for 1080 m; part b is for 1620 m.

Ground-Return Calculations. Based on the above systematics and the calculations in Sec. 3 for the calibration measurements, we can expect that the neutron spectra at the detector will be very sensitive to assumptions about ground scattering and air transport. By themselves, the transmissions as low as 10^{-7} would make a Monte Carlo calculation challenging; adding another factor of about 10^{-7} for the detector solid angle increases the difficulty, especially if representative sampling over the region around the detector is required. Two calculational options have been used to focus separately on the air-transport and ground-scattering issues. To illustrate, **Figs. 4.4a,b** show MCNP4A calculations at the 1080-m (part a) and 1620-m (part b) distances; the error bars on the BC454 data now include the estimated uncertainties from the previous section. The two curves compare the results for a "ring-detector" tally versus a "DXTRAN" sphere. As indicated by the legend, the ring detector ("Open Field") should minimize the influence of local scattering, while the DXTRAN approach ("Ground Return") includes its effect. All calculations use ENDF/B-V cross sections for air transport, and all are averaged over the expected detector resolution of 25–40%.[9] (An input file for the 1080-m ring-detector case is included in **Appendix B.**) The results demonstrate that the energy structure suggested by the measurements is certainly real, and the difference between the two curves emphasizes the effect of ground scattering on the low-energy part of the spectra. Because the direct transmission drops as the distance increases, the differences are larger in the 1620-m spectrum. In both cases, however, the size of the effect introduces new uncertainties in the calculations, especially because of unique features associated with the two measurement sites: the 1080-m position is atop a small hill, and the 1620-m position is in an open field dotted with concrete slabs.

Cross-Section Variations. Alternatively, we can minimize the ground effect by using a ring-detector geometry and instead focus on air transport by switching between the ENDF/B-V and ENDF/B-VI cross-section evaluations. These results are shown in **Figs. 4.5a,b** for the two distances. The effect of the change in cross sections is predominately at high energies, which makes its effect complementary to that for the ground return, which emphasizes lower energies. For both effects, the impact is greatest at the 1620-m distance. Thus, it can be expected that introducing the ground effects and the ENDF/B-VI cross sections together can significantly reduce the calculated spectra at all energies, as shown by the solid curves in **Figs. 4.6a,b.** (The original, unbroadened MCNP4A outputs from these runs are included in **Appendix C.**) For comparison, also shown are similar calculations performed by Science Applications International Corporation (SAIC), using the DORT, two-dimensional discrete-ordinates code, also with ENDF/B-VI cross sections. (A detailed description of these calculations, which were provided by Dean Kaul of SAIC,[28] is included in **Appendix D.**) The agreement between the various measurements and calculations is quite striking, particularly for energies above 2 MeV.

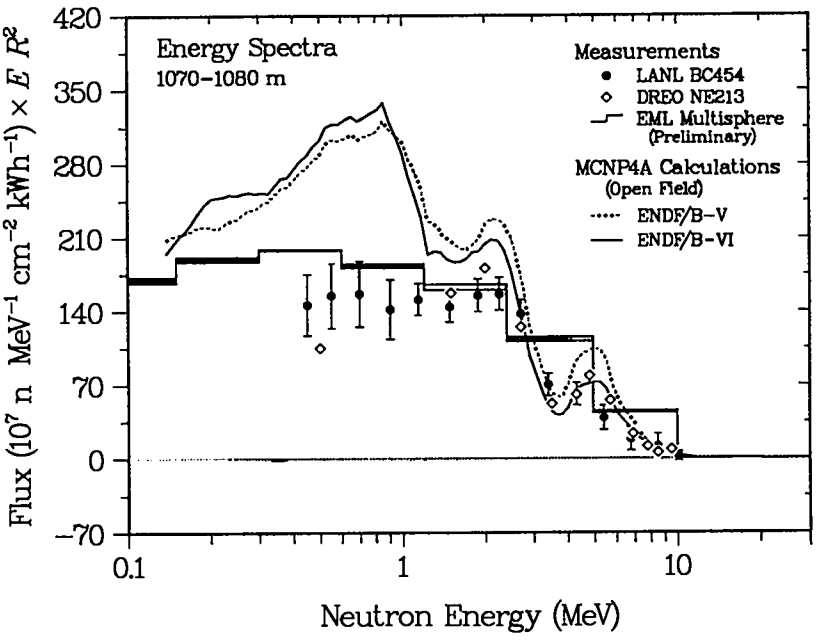

(a)

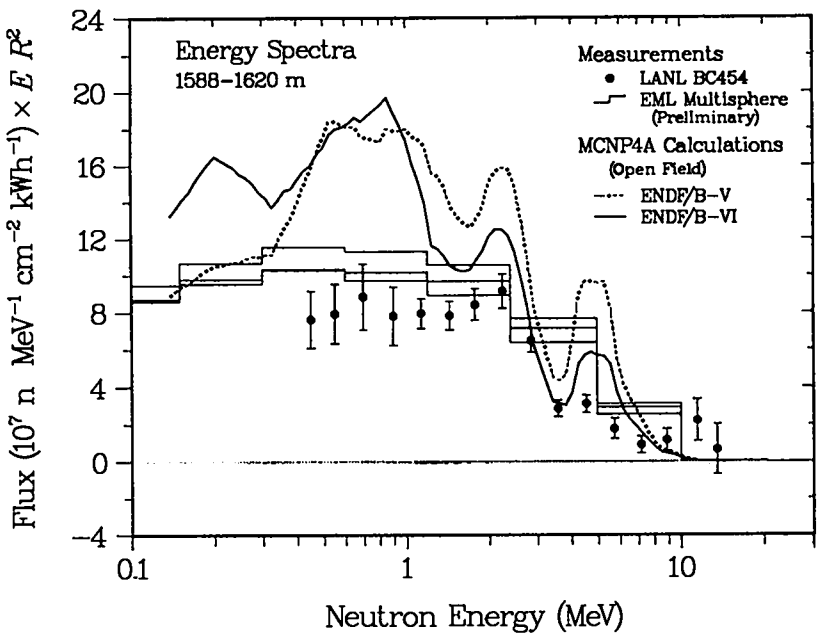

(b)

Figs. 4.5a,b. Comparison between measurements and MCNP4A calculations using either the ENDF/B-V or ENDF/B-VI cross-section libraries. Part a is for 1080 m; part b is for 1620 m.

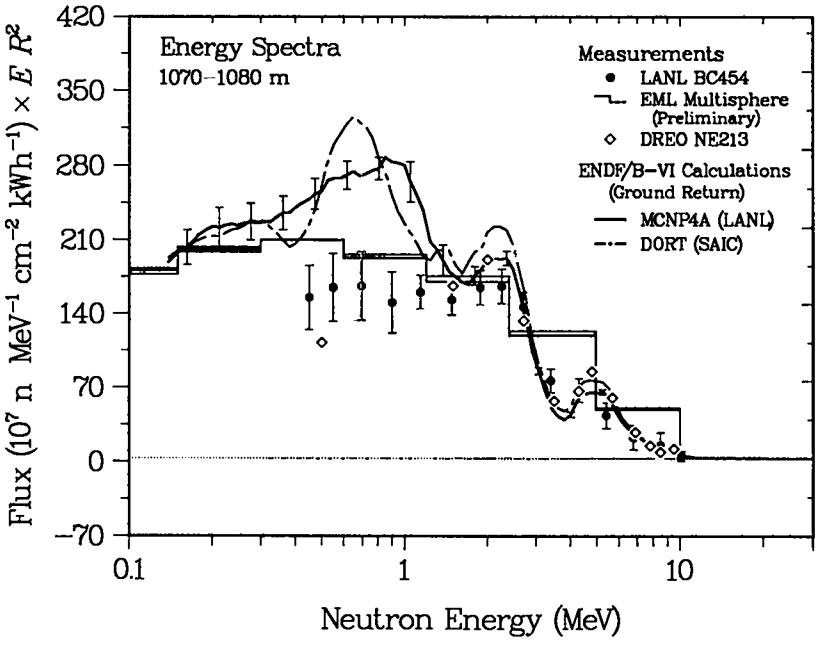

(a)

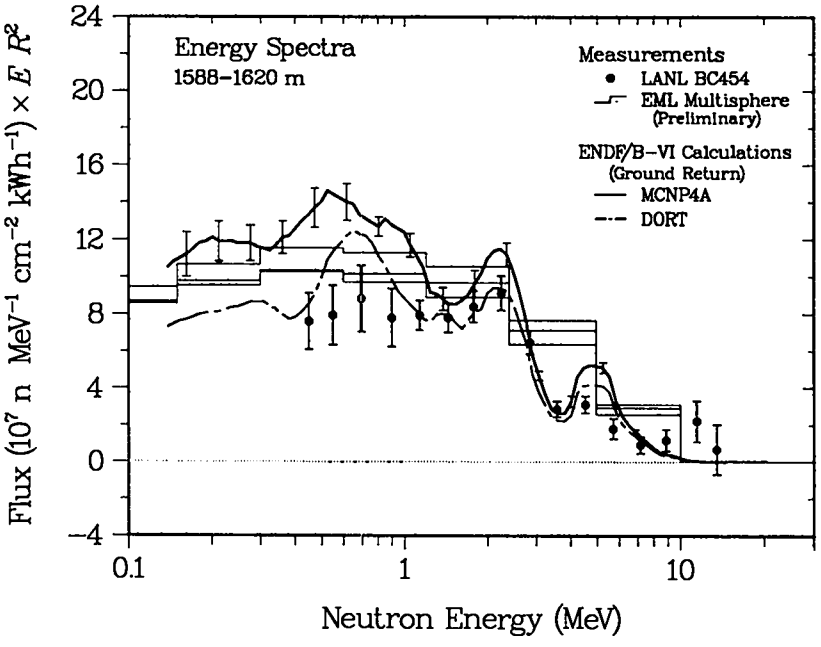

(b)

Figs. 4.6a,b. Comparison between measurements and calculations from the MCNP4A and DORT codes, both including ground scattering and using ENDF/B-VI cross sections. Part a is for 1080 m; part b is for 1620 m.

Analysis Summary. The results in this section provide some insight into the behavior of neutron transport at long ranges. Although the effect is diminished by air and ground scattering, the energy-dependent structure in the nitrogen and oxygen cross sections has a strong influence on the observed spectrum, especially as the direct flux decreases at larger distances. Also significant is the realization that the energy spectrum at the detector is not simply proportional to the original source distribution. In particular, low-energy neutrons from the source, no matter how numerous, are simply not transported to the detector; most of the observed low-energy spectrum is instead associated with higher-energy neutrons that have downscattered in energy, apparently after traveling large distances through a few transmission windows. These air-transport issues combine with the ground-return effects seen in the calibrations to explain the structure in the energy spectra observed at the detector location. The MCNP calculations shown here illustrate this behavior by varying the amount of scattering from the ground near the detector and switching between different cross-section evaluations. The results are similar to those obtained by SAIC calculations using a discrete-ordinates approach, which also accounts for ground return near the detector. The final collection of measurements and calculations is summarized as differential dose spectra in **Fig. 4.7**, which shows the 1080-m and 1600-m data sets normalized by the ratio of the integral dose values. (For the preliminary Multisphere data, only the extreme values are shown.) Both the measurements and the calculations have the same behavior, with a gradual hardening of the spectra with increasing range. Overall, the agreement between different determinations of the fast-neutron spectra is very satisfactory.

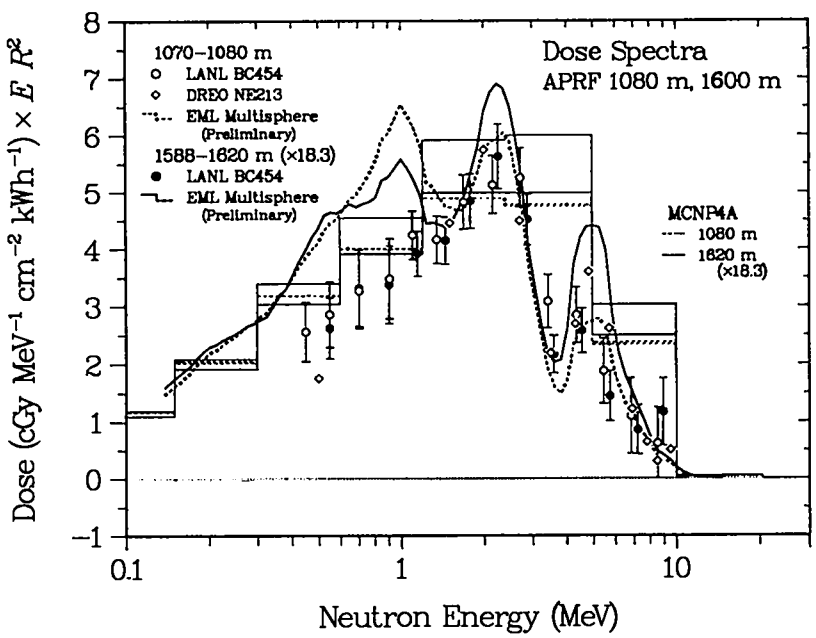

Fig. 4.7. Differential neutron-dose distributions at 1070–1080 m and 1588–1620 m, showing both measurements and calculations. The 1600-m values have been rescaled by a factor of 18.3.

5. SUMMARY

Boron-Loaded Neutron Spectrometers. Much of this report (Sec. 2) discusses the operation of the unique neutron detector used in these measurements. The diagnostics provided by the exponential dependence of the capture times and the characteristic light-output spectrum for the capture pulse ensure that only fast neutrons are included in the final energy spectra. Also of importance for the present work is the internal light-output calibration provided by the standard shape of the second-pulse spectrum, which establishes the neutron energy scale. Finally, the normalization for the measurements, which depends on the demonstrated connection between the source calibrations and the reactor measurements, is supported by the agreement between analyses using either measured or calculated efficiencies and between the results for one-rod, two-rod, and four-rod summations over the multielement detector.

Directional Measurements. A unique feature of the detector is its capability for determining the average direction of the incident neutron flux by using ratios of count rates in different elements. This option was demonstrated by using source calibrations with two detector orientations that were rotated by 45°. In the reactor results, this directional capability yielded measured polarizations of 0.36 ± 0.04 and apparent source angles of $35 \pm 4°$ above the horizon. Within the uncertainties, these observations can be reproduced by simple MCNP calculations. This insight helps in visualizing the radiation field at the detector in terms of the relative amounts of direct and skyshine contributions.

Room, Air, and Ground Scattering. Central to our understanding of the measured spectra is the relative importance of the direct and scattered fluxes as seen in the ^{252}Cf source calibrations. First, floor or ground scattering must be included to obtain the correct absolute calibration of the instrument. Second, the consistent agreement between measurements and calculations, both indoor and outdoor and at 1-m and 2-m separations, lends strong support to the reliability of both the measurements and the Monte Carlo calculations used throughout our analyses.

Far-Field Fast-Neutron Measurements and Calculations. The agreement between the calibrations and calculations leads to the central measurements in the present work, fast-neutron reactor spectra at distances of 1080 m and 1620 m. At the shorter distance, the present BC454 scintillator results are in excellent agreement with earlier NE213 proton-recoil data. At both distances the reported magnitudes are supported to within about 30–50% by the preliminary Multisphere data. When the different data sets are taken together, there is consensus within about ±20% for the fast-neutron spectrum from 0.5 to 10 MeV. In addition, reasonable extensions to lower energies provide integral doses that also agree with recent measurements.

Long-Range Air-over-Ground Transport. Our final section examines in some detail the behavior of fast-neutron transport at large ranges. The analyses reveal the importance of cross-section windows in explaining the observed energy spectra, the dominance of scattered over direct contributions, and the large leverage associated with source neutrons at the highest energies. These considerations preface the comparisons between the measurements and transport calculations, which illustrate the effects of different assumptions about ground scattering near the the detector and changes in the cross sections used for air transport. Above 2 MeV, the measurements are reproduced within their uncertainties; below this energy, variations between different calculations of the ground return limit the agreement to about 20%.

Conclusions. Our goal in this work was to provide a set of fast-neutron spectral measurements at large distances from the APRF reactor, which could then provide a benchmark

for neutron-transport calculations of the effect of the air-over-ground interface on long-range neutron dosimetry at Hiroshima and Nagasaki. Our results demonstrate both the agreement between the different experimental techniques and between the resulting measurements and state-of-the-art transport calculations, at least when care is taken with local scattering effects and when the most recent cross-section evaluations are included. This agreement testifies to the accuracies of the calculational models and the technology of the neutron spectrometer, which is expected to provide new capabilities for field measurements of neutron sources.

ACKNOWLEDGMENTS

Catherine Mannon, a science teacher in Albuquerque, New Mexico, was sponsored for this work by LANL's Nonproliferation and International Security Division. This report includes the results of her research on neutron dosimetry, which she will continue further as she works with teachers from Russia, Mexico, and throughout the United States to help students better understand issues in science and technology.

This work was supported as part of the Field Neutron Spectrometer project being carried out by the Research and Technology Division of the DOE's Office of Nonproliferation and National Security. At LANL, the original measurements were encouraged by Paul Whalen, and arrangements for transporting the detector and calibration source to APRF were made by George Auchampaugh. The MCNP4A code is a product of the Radiation Transport Group and was obtained from John Hendricks. At APRF, experimental support was provided by Richard Harrison, Craig Heimbach, and John Gerdes. Valuable discussions about the various calculations and measurements also involved Craig Heimbach of APRF, Dean Kaul of SAIC, and Paul Goldhagen of DOE/EML.

REFERENCES

1. J. A. Auxier, "ICHIBAN: Radiation Dosimetry for the Survivors of the Bombings of Hiroshima and Nagasaki," Department of Energy report TID-27080 (1977).
2. W. C. Roesch, Ed., *US–Japan Joint Reassessment of Atomic Bomb Radiation Dosimetry in Hiroshima and Nagasaki* (The Radiation Effects Research Foundation, Hiroshima, Japan, 1987).
3. T. Straume et al., "Neutrons Discrepancies in the DS86 Hiroshima Dosimetry System," *Health Physics* **64** 421 (1994); or T. Straume et al., "Neutrons Confirmed in Nagasaki and APRF: Implications for Hiroshima," *Radiation Research* **138(2)**, 193–200 (1994).
4. P. P. Whalen, "Source and Replica Calculations," in *Proceedings of the 8th International Conference on Radiation Shielding* (American Nuclear Society, Inc., La Grange Park, Illinois, 1994), pp. 212–223.
5. D. C. Kaul, W. A. Woolson, S. D. Egbert, and T. Straume, "A Brief Summary of Comparisons Between the DS86 A-Bomb Survivor Dosimetry System and In-Situ Measurements in Light of New Measurements, Revised Nuclear Data and Improved Calculational Methods," in *Proceedings of the 8th International Conference on Radiation Shielding* (American Nuclear Society, Inc., La Grange Park, Illinois, 1994), pp. 232–237.
6. A. H. Kazi, C. R. Heimbach, R. C. Harrison, and H. A. Robitaille, "Comparison of Measured and Calculated Radiation Transport in Air-Over-Ground Geometry to 1.6 km from a Fission Source," *Nuclear Science and Engineering* **85**, 371–386 (1983).
7. W. C. Feldman, G. F. Auchampaugh, and R. C. Byrd, "A Novel Fast Neutron Detector for Space Applications," *Nuclear Instruments and Methods* **A306**, 350–365 (1991).
8. Roger C. Byrd, George F. Auchampaugh, and William C. Feldman, "Measurement and Analysis of Neutron Energy Spectra from Fission Sources," Los Alamos National Laboratory report LA-12627-MS (November 1993).

9. R. C. Byrd and W. T. Urban, "Calculations of the Neutron Response of Boron-Loaded Scintillators," Los Alamos National Laboratory report LA-12833-MS (December 1994).
10. M. E. Toms, "A Computer Analysis to Obtain Neutron Spectra from an Organic Scintillator," *Nuclear Instruments and Methods* **92**, 61–70 (1971).
11. D. Slaughter and R. Strout II, "FLYSPEC: A Simple Method of Unfolding Neutron Energy Spectra Measured with NE213 and Stilbene Spectrometers," *Nuclear Instruments and Methods* **198**, 349–355 (1982).
12. R. L. Bramblett, R. I. Ewing, and T. W. Bonner, "A New Type of Neutron Spectrometer," *Nuclear Instruments and Methods* **9**, 1–12 (1960).
13. D. D. Drake, W. C. Feldman, and C. Hurlbut, "New Electronically Black Neutron Detectors," *Nuclear Instruments and Methods* **A247**, 576–582 (1986).
14. R. C. Byrd, G. F. Auchampaugh, C. E. Moss, and W. C. Feldman, "Warhead Counting Using Neutron Scintillators: Detector Development, Testing, and Demonstration," *IEEE Transactions on Nuclear Science* **NS-39**, 1051–1055 (August 1992).
15. C. E. Moss, R. C. Byrd, G. F. Auchampaugh, W. C. Feldman, G. P. Estes, R. I. Ewing, and K. W. Marlow, "Detection of Uranium-Based Nuclear Weapons Using Neutron-Induced Fission," in *Conference Record of the 1991 IEEE Nuclear Science Symposium and Medical Imaging Conference* (The Institute of Electrical and Electronics Engineers, Piscataway, New Jersey, 1991), pp. 1218–1221.
16. R. C. Byrd, "Directional Fast-Neutron Detectors," Los Alamos National Laboratory report LA-12379-MS (October 1992).
17. Roger C. Byrd, George F. Auchampaugh, and William C. Feldman, "Directional Measurements for Sources of Fission Neutrons," Los Alamos National Laboratory report LA-12633-MS (November 1993).
18. R. Madey, F. M. Waterman, A. R. Baldwin, J. N. Knudson, J. D. Carlson, and J. Rapaport, "The Response of NE-228A, NE-228, NE-224, and NE-102 Scintillators to Protons from 2.43 to 19.55 MeV," *Nuclear Instruments and Methods* **151**, 445 (1978).
19. F. H. Fröhner, "Evaluation of ^{252}Cf Prompt Fission Neutron Data from 0 to 20 MeV by Watt Spectrum Fit," *Nuclear Science and Engineering* **106**, 345–352 (1990).
20. R. C. Byrd, J. D. Drabanski, and B. L. Barraclough, "Monte Carlo Calculations of the Effective Area and Directional Response of a Polyethylene-Moderated Neutron Counter," Los Alamos National Laboratory report LA-12850-MS (January 1995).
21. E. C. Torres, "Report of Calibration," Los Alamos National Laboratory notebook no. R-6509, pp. 118–119 (November 20, 1992).
22. W. C. Feldman et al., "Calibration of a Space Thermal/Epithermal Neutron Detector: The Mars Observer Gamma-Ray Spectrometer Anticoincidence Shield," *Nuclear Instruments and Methods* (submitted).
23. J. F. Briesmeister, Ed., "MCNP–A General Monte Carlo N-Particle Transport Code, Version 4A," Los Alamos National Laboratory report LA-12625-M (November 1993).
24. Craig Heimbach, Army Pulse Radiation Facility, private communication, 1994.
25. C. R. Heimbach, M. A. Oliver, and M. B. Stanka, "Long-Distance Air-Over-Ground Transport of Radiation," in *Proceedings of the 8th International Conference on Radiation Shielding* (American Nuclear Society, Inc., La Grange Park, Illinois, 1994), pp. 1079–1085.
26. G. P. Estes, R. C. Little, R. E. Seamon, and P. D. Soran, "Air Transport in Connection with the Hiroshima-Nagasaki Dose Reevaluation Effort," Los Alamos National Laboratory report LA-9369-MS (July 1982).
27. Paul Goldhagen, Department of Energy/Environmental Measurements Labratory, private communication, 1994.
28. Dean Kaul, Science Applications International Corporation, private communication, 1994.

Appendix A. Present Measurements

1080 m

Energies (MeV) Mean	Upper	Flux $(\text{n}\cdot\text{MeV}^{-1}\cdot\text{cm}^{-2}\cdot\text{kWh}^{-1}) \times R^2$	Fractional Error
0.45	0.50	0.3250E+10	0.034
0.55	0.64	0.2822E+10	0.044
0.70	0.80	0.2229E+10	0.041
0.91	1.01	0.1570E+10	0.043
1.15	1.27	0.1311E+10	0.039
1.50	1.60	0.9617E+09	0.046
1.90	2.02	0.8161E+09	0.061
2.26	2.54	0.6939E+09	0.083
2.72	3.19	0.5036E+09	0.073
3.42	4.02	0.2028E+09	0.146
4.34	5.06	0.1408E+09	0.186
5.44	6.37	0.7130E+08	0.309
6.82	8.02	0.2779E+08	0.637
8.55	10.1	0.1402E+08	1.033

1620 m

Energies (MeV) Mean	Upper	Flux $(\text{n}\cdot\text{MeV}^{-1}\cdot\text{cm}^{-2}\cdot\text{kWh}^{-1}) \times R^2$	Fractional Error
0.45	0.50	0.1694E+09	0.026
0.55	0.64	0.1442E+09	0.031
0.70	0.80	0.1262E+09	0.025
0.90	1.01	0.8623E+08	0.031
1.15	1.27	0.6992E+08	0.030
1.45	1.60	0.5408E+08	0.038
1.79	2.02	0.4726E+08	0.041
2.26	2.54	0.4042E+08	0.045
2.87	3.19	0.2241E+08	0.065
3.59	4.02	0.7919E+07	0.154
4.55	5.06	0.6908E+07	0.153
5.75	6.37	0.3170E+07	0.274
7.20	8.02	0.1275E+07	0.600
8.93	10.1	0.1372E+07	0.517
11.53	12.4	0.1945E+07	3.639
13.50	15.7	0.4997E+06	1.666

Appendix B. MCNP Input File, 1080 m

The cell and surface cards lay out a cylindrically symmetric geometry with the air region composed of hemispheres with increasing radii (surfaces 1–9) split into three conical slices (surfaces 15–16). The ring detector at 1080 m is located in the lowest conical slice, between the 1000-m and 1200-m radii at surfaces 5 and 6. The soil region consists of concentric rings at the depths specified by surfaces 10–14, which extend down to a depth of 24 cm. The air (material 1) has a density of 1.23 mg/cm^3 and is 78.78% nitrogen, 20.21% oxygen, and 1.01% hydrogen (by number), which corresponds to about 0.6% water (by weight). The ground has a density of 1.9 g/cm^3 and is about 20% water by weight.

```
m11a w/ dd .95 1000
c    converted to mcnpv4a 8/1/94, added large outer cell
c
c      cell cards for air
c
1    1 -1.23e-3 -1 10
2    1 -1.23e-3 1 -2 10 16
3    1 -1.23e-3 1 -2 10 15 -16
4    1 -1.23e-3 1 -2 10 -15
5    1 -1.23e-3 2 -3 10 16
6    1 -1.23e-3 2 -3 10 15 -16
7    1 -1.23e-3 2 -3 10 -15
8    1 -1.23e-3 3 -4 10 16
9    1 -1.23e-3 3 -4 10 15 -16
10   1 -1.23e-3 3 -4 10 -15
11   1 -1.23e-3 4 -5 10 16
12   1 -1.23e-3 4 -5 10 15 -16
13   1 -1.23e-3 4 -5 10 -15
14   1 -1.23e-3 5 -6 10 16
15   1 -1.23e-3 5 -6 10 15 -16
16   1 -1.23e-3 5 -6 10 -15
17   1 -1.23e-3 6 -7 10 16
18   1 -1.23e-3 6 -7 10 15 -16
19   1 -1.23e-3 6 -7 10 -15
20   1 -1.23e-3 7 -8 10 16
21   1 -1.23e-3 7 -8 10 15 -16
22   1 -1.23e-3 7 -8 10 -15
23   1 -1.23e-3 8 -9 10 16
24   1 -1.23e-3 8 -9 10 15 -16
25   1 -1.23e-3 8 -9 10 -15
c
c      cell cards for ground
c
26   2 -1.9 -1 11 -10
27   2 -1.9 -1 12 -11
28   2 -1.9 -1 13 -12
29   2 -1.9 -1 14 -13
30   2 -1.9 1 -2 11 -10
31   2 -1.9 1 -2 12 -11
32   2 -1.9 1 -2 13 -12
33   2 -1.9 1 -2 14 -13
34   2 -1.9 2 -3 11 -10
35   2 -1.9 2 -3 12 -11
36   2 -1.9 2 -3 13 -12
37   2 -1.9 2 -3 14 -13
38   2 -1.9 3 -4 11 -10
39   2 -1.9 3 -4 12 -11
```

```
40   2 -1.9 3 -4 13 -12
41   2 -1.9 3 -4 14 -13
42   2 -1.9 4 -5 11 -10
43   2 -1.9 4 -5 12 -11
44   2 -1.9 4 -5 13 -12
45   2 -1.9 4 -5 14 -13
46   2 -1.9 5 -6 11 -10
47   2 -1.9 5 -6 12 -11
48   2 -1.9 5 -6 13 -12
49   2 -1.9 5 -6 14 -13
50   2 -1.9 6 -7 11 -10
51   2 -1.9 6 -7 12 -11
52   2 -1.9 6 -7 13 -12
53   2 -1.9 6 -7 14 -13
54   2 -1.9 7 -8 11 -10
55   2 -1.9 7 -8 12 -11
56   2 -1.9 7 -8 13 -12
57   2 -1.9 7 -8 14 -13
58   2 -1.9 8 -9 11 -10
59   2 -1.9 8 -9 12 -11
60   2 -1.9 8 -9 13 -12
61   2 -1.9 8 -9 14 -13
62   1 -1.23e-3 9 -99 14   $outside air,
63   0 99:-14

c
c      surface cards
c
1    so 20000
2    so 40000
3    so 60000
4    so 80000
5    so 100000
6    so 120000
7    so 140000
8    so 160000
9    so 180000
10   pz 0
11   pz -6.
12   pz -12
13   pz -18
14   pz -24
15   kz 0 .33333 1
16   kz 0 3 1
99   so 500000

mode n
imp:n 32 64 32 16 128 32 8 256 32 4 512 32 2
      1028 32 1 512 32 1 256 32 1 128 32 1
      64 32 16 8   128 64 32 16   256 128 64 32
      512 256 128 64   1024 512 256 128   2048 1024 512 256
      1024 512 256 128   512 256 128 64   256 128 64 32
      32 0   $outside
c
c      source cards
c
sdef pos=0 0 1400   cel=1   wgt=1  erg=d1
```

```
si1  1.013e-4 5.829e-4 1.234e-3 3.355e-3 1.033e-2 2.188e-2 2.479e-2
     5.248e-2 1.111e-1 .1576 .5502 1.108 1.827 2.307 2.385 3.012
     4.066 4.724 4.965 6.376 7.408 8.187 9.048 10 11.05 12.21
     12.84 13.84 14.19 14.92 16.9
sp1  0 1.e-5 3.e-5 1.6e-4 8.9e-4 2.54e-3 6.7e-4 8.91e-3
     2.483e-2 2.46e-2 .2581 .2376 .175 7.637e-2 1.058e-2
     6.184e-2 5.892e-2 2.068e-2 5.47e-3 2.059e-2 6.19e-3 2.63e-3
     1.59e-3 9.8e-4 4.5e-4 2.3e-4 7.e-5 6.e-5 2.e-5 2.e-5
     1.e-5
sb1   0 100 97 94 91 88 85 82 79 76 73 70
           67 64 61 58 55 52 49 56 43 40 37 34 31 28 25 22 19 16 13
c
c      detector cards
c
f5z:n  155 108000 155
fc5  neutron flux at 1080 meters
c
dd   .95 1000
e0   .01585 .02512 .03981 .06310  .10
      .1585  .2512  .3981  .6310 1.0
      1.2 1.4 1.6 1.8 2.0
      2.2 2.4 2.6 2.8 3.0
      3.2 3.4 3.6 3.8 4.0
      4.2 4.4 4.6 4.8 5.0
       5.5  6  6.5  7  7.5  8  8.5  9  9.5 10
      10.5 11 11.5 12 12.5 13 13.5 14 14.5 15
      15.5 16 16.5 17 17.5 18 18.5 19 19.5 20
c
c      material cards
c
m1   7014.50 .7878 8016.50 .2021 1001.50 .0101   $rh=74,byrd weather
m2    1001 3.01-2  8016 5.32-2 11023 2.60-4   $aprd gnd, dry, rho=-1.9
     13027 1.30-3 14000 1.90-2 26000 3.50-4   $aprd gnd, dry, rho=-1.9
c
c     thermal cards
c
cut:n 1.e+123 .010 -.5 -.25
c    ergn -15 20
phys:n 20 j
print
nps  300000
```

1080 m

Midpoint Energies (MeV)	Flux $(\text{n}\cdot\text{MeV}^{-1}\cdot\text{cm}^{-2}\cdot\text{kWh}^{-1}) \times R^2$	Fractional Error
0.13	0.175E+10	0.083
0.20	0.212E+10	0.084
0.32	0.213E+10	0.071
0.51	0.247E+10	0.053
0.82	0.266E+10	0.038
1.10	0.219E+10	0.108
1.30	0.181E+10	0.057
1.50	0.153E+10	0.059
1.70	0.153E+10	0.057
1.90	0.151E+10	0.044
2.10	0.204E+10	0.040
2.30	0.207E+10	0.033
2.50	0.157E+10	0.028
2.70	0.145E+10	0.030
2.90	0.857E+09	0.039
3.10	0.484E+09	0.043
3.30	0.315E+09	0.060
3.50	0.289E+09	0.085
3.70	0.326E+09	0.080
3.90	0.413E+09	0.070
4.10	0.361E+09	0.062
4.30	0.307E+09	0.058
4.50	0.429E+09	0.047
4.70	0.109E+10	0.027
4.90	0.115E+10	0.024
5.25	0.490E+09	0.043
5.75	0.344E+09	0.050
6.25	0.300E+09	0.043
6.75	0.279E+09	0.033
7.25	0.103E+09	0.046
7.75	0.676E+08	0.046
8.25	0.971E+08	0.043
8.75	0.739E+08	0.055
9.25	0.447E+08	0.047
9.75	0.257E+08	0.057
10.30	0.104E+08	0.063
10.80	0.959E+07	0.059
11.30	0.645E+07	0.092
11.80	0.455E+07	0.088
12.30	0.283E+07	0.097
12.80	0.210E+07	0.109
13.30	0.160E+07	0.111
13.80	0.118E+07	0.131
14.30	0.499E+06	0.179
14.80	0.223E+06	0.252
15.30	0.200E+06	0.315
15.80	0.141E+06	0.333
16.30	0.114E+06	0.345
16.80	0.822E+05	0.580

1620 m

Midpoint Energies (MeV)	Flux $(\mathrm{n \cdot MeV^{-1} \cdot cm^{-2} \cdot kWh^{-1}}) \times R^2$	Fractional Error
0.13	0.104E+09	0.119
0.20	0.121E+09	0.089
0.32	0.113E+09	0.070
0.51	0.143E+09	0.077
0.82	0.129E+09	0.039
1.10	0.944E+08	0.071
1.30	0.899E+08	0.066
1.50	0.820E+08	0.067
1.70	0.756E+08	0.075
1.90	0.111E+09	0.080
2.10	0.116E+09	0.071
2.30	0.134E+09	0.040
2.50	0.975E+08	0.042
2.70	0.831E+08	0.033
2.90	0.452E+08	0.058
3.10	0.309E+08	0.068
3.30	0.202E+08	0.084
3.50	0.195E+08	0.092
3.70	0.212E+08	0.092
3.90	0.295E+08	0.096
4.10	0.296E+08	0.078
4.30	0.336E+08	0.128
4.50	0.413E+09	0.089
4.70	0.104E+09	0.044
4.90	0.105E+09	0.036
5.25	0.349E+08	0.059
5.75	0.249E+08	0.057
6.25	0.236E+08	0.048
6.75	0.217E+08	0.036
7.25	0.561E+07	0.050
7.75	0.528E+07	0.086
8.25	0.660E+07	0.040
8.75	0.510E+07	0.061
9.25	0.280E+07	0.047
9.75	0.147E+07	0.047
10.30	0.558E+06	0.078
10.80	0.477E+06	0.067
11.30	0.292E+06	0.063
11.80	0.223E+06	0.118
12.30	0.131E+06	0.117
12.80	0.712E+05	0.157
13.30	0.506E+05	0.082
13.80	0.417E+05	0.129
14.30	0.313E+05	0.134
14.80	0.114E+05	0.136
15.30	0.442E+04	0.210
15.80	0.436E+04	0.257
16.30	0.106E+04	0.490
16.80	0.103E+04	0.677

Appendix D. DORT Calculations

Calculations of neutron and gamma-ray fluences about the APRF reactor were performed by Science Applications International Corporation, using the DORT two-dimensional discrete-ordinates code, which is part of the DOS discrete-ordinates system (Ref. D1). The cross sections used in the calculation were taken primarily from the VITAMIN-B6 fine-group (energy interval) cross-section set, consisting of 199 neutron groups in approximately equal lethargy intervals from 10^{-4} eV to 20 MeV, including 30 groups with upscatter below approximately 5 eV, and 42 gamma-ray groups from 0.01 to 20 MeV (Ref. D2). The source was taken from a 1990 revision of the SAIC 1989 calculation of energy- and angle-differential leakage of neutrons and gamma rays from the APRF reactor (Ref. D3). The primary effect of that revision was to change the emission rate from 1.26×10^{17} n·kWh^{-1} to 1.295×10^{17} n·kWh^{-1}.

The DORT calculations were performed in cylindrical (r-z) geometry, using an $S8$ angular quadrature, expanded from 48 angles to 240 angles by subdividing each angle into 5, all in the polar direction. This quadrature virtually eliminates the propensity of radiation to move preferentially along quadrature directions, that is, so-called ray effects. The calculations used a Legendre scattering order of 3. The geometry represented in the calculations consisted of 1500 m of air over 1 m of ground, represented in 102 axial mesh intervals, extending to a radius of 2900 m, represented in 123 radial mesh intervals. The primary mesh dimension was 25 m. The air constituents included nitrogen, oxygen, and argon, plus moisture at 1% of total density, which was 1.233 mg/cm^3. The ground contained moisture at 30% of dry density. The total ground density was 1.7 g/cm^3.

References

D1. W. A. Rhoades and M. B. Emmett, "DOS: The Discrete Ordinates System," Oak Ridge National Laboratory report ORNL/TM-8362 (1982).

D2. D. T. Ingersoll, J. E. White, R. Q. Wright, H. T. Hunter, C. O. Slater, N. M. Greene, R. E. MacFarlane, and R. W. Rousin, "Production and Testing of the VITAMIN-B6 Fine Group and the BUGLE-93 Broad Group Neutron/Photon Cross-Section Libraries Derived from ENDF/B-VI Nuclear Data," Oak Ridge National Laboratory report ORNL-6795 (Draft) (April 1994).

D3. D. C. Kaul and S. D. Egbert, "Radiation Leakage from the Army Pulse Radiation Facility (APRF) Fast Reactor," Science Applications International Corporation, San Diego, California, report SAIC-89/1423 (12 May 1989).

•U.S. GOVERNMENT PRINTING OFFICE 1995-0-673-021/7077

Los Alamos
NATIONAL LABORATORY
Los Alamos, New Mexico 87545